International Journal of Plasticity 26 (2010) 1485–1507

Contents lists available at ScienceDirect

International Journal of Plasticity

journal homepage: www.elsevier.com/locate/ijplas

Three-dimensional modeling and numerical analysis of rate-dependent irrecoverable deformation in shape memory alloys

Darren J. Hartl, George Chatzigeorgiou, Dimitris C. Lagoudas *

Department of Aerospace Engineering, Texas A&M University, 3409 TAMU College Station, TX 77843-3409, USA

ARTICLE INFO

Article history:
Received 7 October 2009
Received in final revised form 29 December 2009
Available online 25 January 2010

Keywords:
Shape memory alloy
High temperature shape memory alloy
Constitutive modeling
Viscoplasticity
Finite element analysis

ABSTRACT

Shape memory alloys (SMAs) provide an attractive solid-state actuation alternative to engineers in various fields due to their ability to exhibit recoverable deformations while under substantial loads. Many constitutive models describing this repeatable phenomenon have been proposed, where some models also capture the effects of rate-independent irrecoverable deformations (i.e., plasticity) in SMAs. In this work, we consider a topic not addressed to date: the generation and evolution of irrecoverable viscoplastic strains in an SMA material. Such strains appear in metals subjected to sufficiently high temperatures. The need to account for these effects in SMAs arises when considering one of two situations: the exposure of a conventional SMA material (e.g., NiTi) to high temperatures for a non-negligible amount of time, as occurs during shape-setting, or the utilization of new high temperature shape memory alloys (HTSMAs), where the elevated transformation temperatures induce transformation and viscoplastic behaviors simultaneously. A new three-dimensional constitutive model based on established SMA and viscoplastic modeling techniques is derived that accounts for these behaviors. The numerical implementation of the model is described in detail. Several finite element analysis (FEA) examples are provided, demonstrating the utility of the new model and its implementation in assessing the effects of viscoplastic behaviors in shape memory alloys.

1. Introduction

From among the various types of active materials described in the literature (Srinivasan and McFarland, 2000), researchers have established shape memory alloys (SMAs) as an optimal design solution to many engineering problems for their ability to exhibit fully recoverable deformations while under substantial loads (Perkins, 1975). Those in the aerospace, medical, and petroleum industries, among others, have investigated the advantages of SMA applications as enabling technologies (Lagoudas, 2008). The mechanism underlying this repeatable response is a solid-to-solid martensitic phase transformation, where the response is rate-independent at most engineering time scales due to the diffusionless nature of the transformation (Otsuka and Wayman, 1999).

While a number of complexities and intricacies have yet to be addressed, the phenomenological modeling of the reversible martensitic transformation under the most common loading conditions has been well established. Combination, alteration, and permutation of established methods of mechanics, especially those related to rate-independent inelastic phenomena, have served to provide the community with a plethora of modeling options for the conventional transformation response, too numerous to recall here. For a review of these options, the reader is referred to the works of Birman (1997),

---

* Corresponding author.
E-mail address: lagoudas@tamu.edu (D.C. Lagoudas).
URL: http://www.smart.tamu.edu (D.C. Lagoudas).

0749-6419/$ - see front matter © 2010 Elsevier Ltd. All rights reserved.
doi:10.1016/j.ijplas.2010.01.002

Patoor et al. (2006), Lagoudas et al. (2006) and Paivia and Savi (2006). Some of the most commonly cited 1-D models that account for the recoverable inelastic strains in SMAs include those of Tanaka et al. (1986), Brinson (1993) and Ivshin and Pence (1994). The first known 3-D phenomenological model for SMAs was that described by Bertram in 1982 (Bertram, 1982), though this is rarely acknowledged; the 3-D models discussed most often in the literature are those of Boyd and Lagoudas (1996), Auricchio et al. (1997), and Raniecki and Lexcellent (1998).

Moving beyond the conventional and repeatable response of SMAs, the generation and evolution of *irrecoverable* deformations in SMAs have also been considered. Researchers such as Lagoudas and Entchev (2004) have studied and modeled transformation-induced plasticity (TRIP), in which plastic strains are generated in each transformation cycle, even when load levels are moderate. The works of others such as Paiva et al. (2005), Yan et al. (2003), Wang et al. (2008), Zhang et al. (2007) and Hartl and Lagoudas (2009) have also examined high-stress rate-independent yielding plasticity in SMAs that occurs when local resolved stresses exceed those required to initiate slip. The work of Hartl and Lagoudas (2009), for example, considers the simultaneous evolution of transformation and plastic strains.

In this work, we consider a topic that has not been addressed in the SMA modeling community to date: a new class of irrecoverable deformations that are described by the rate-dependent, diffusion-driven viscoplastic strains induced by the processes of climb and other motion of vacancies or dislocations (Lemaitre and Chaboche, 1990). Such strains appear and evolve in metals subjected to sufficiently high temperatures (greater than roughly one-third the absolute melting temperature). The need to account for these effects in shape memory alloys arises from one of the following two engineering problems: (i) assessment of the change in thermomechanical state and change in actuation behavior for a *conventional SMA material* (transformation temperatures below 100 °C) that has been exposed to high temperatures and sufficient forces due to processing, shape-setting, or other processes, or (ii) assessment of the coupled transformation–viscoplastic yielding response of a high temperature shape memory alloy (HTSMA) with transformation temperatures sufficiently high to induce viscoplastic deformations. To predict the structural response of both conventional SMAs at elevated temperatures in addition to the newer HTSMA compositions providing actuation, the new constitutive model described in this work is needed.

Clearly the processing, shape setting, and application of conventional SMAs is an established subject with a long history (Otsuka and Wayman, 1999). The rate-dependent viscoplastic behavior of conventional SMA compositions such as NiTi exposed to high temperatures has been experimentally studied, and creep has been observed and quantified given both tensile (Mukherjee, 1968; Eggeler et al., 2002; Lexcellent et al., 2005) and compressive loads (Oppenheimer et al., 2007). However, the temperatures required to induce such diffusion-driven rate-dependency far exceed the useful actuation or pseudoelastic temperature range of conventional SMA materials, though such temperatures are applied during metal forming, processing, and shape-setting. To date, the consequences of high temperature excursions on components composed of these conventional SMA materials have not been modeled, and this is an important contribution of this work.

More recently, however, the range of SMA research topics from alloy development (Padula et al., 2006) to basic material characterization (Kumar and Lagoudas, 2009) to application design (Noebe et al., 2006) has found a new focus in HTSMAs. Potential HTSMA applications have been investigated for the oil and aerospace industries. For example, jet engine chevrons have been proposed for installation in the engine core region, where the high temperatures of engine exhaust require transformation temperatures far above that observed in conventional SMAs (Noebe et al., 2006). In such an application, it is important to understand how the high ambient temperatures will effect the operation of the active structure, and how that operation might change over time or actuation cycles. The ability to capture the coupled processes (transformation and viscoplastic deformations) simultaneously is becoming increasingly important, especially to predict the actuation loss that can occur in these materials due to the irrecoverable rate-dependent strains.

It is worth reviewing briefly that the rate-dependency of SMAs is not limited to high temperature, diffusion-driven behaviors. In studying the effects of loading rate on the stress–strain response, some works have considered tensile testing at rates exceeding conventional quasi-static levels (Shaw and Kyriakides, 1995; Grabe and Bruhns, 2008), while others have investigated dynamic loading conditions (i.e., impact loading) (Escobar and Clifton, 1993; Popov et al., 2003; Liu et al., 2002). The results of these studies indicate that the stress–strain response during austenite–martensite transformation is clearly rate-dependent. This is attributed to the coupling between the latent heat of martensitic transformation and the variation of transformation stress with temperature (Boyd and Lagoudas, 1996; Lexcellent and Rejzner, 2000). This rate-dependency is then accounted for by coupling the first law of thermodynamics and heat transfer mechanisms with the proposed thermomechanical constitutive equations. It is not related to the classical metal viscoplasticity described in this work.

Several rate-dependent models have been proposed in order to simulate the coupled thermomechanical behavior of SMAs (e.g., pseudoelasticity, shape memory effect). Rate-dependent lumped parameter models have been introduced for vibration damping, assuming various forms of the structural damping of SMA devices (Fosdick and Ketema, 1998). Several SMA models capturing rate-dependent behavior are introduced as methods to account for the rate-dependent thermal effects associated with the latent heat of transformation (Făciu and Mihăilescu-Suliciu, 2002; Auricchio et al., 2008). However, none of these modeling tools are applicable to the problem of rate-dependent irrecoverable (i.e., viscoplastic) strains; the previously proposed formulations apply only to the physical process of phase transformation and include only elastic and recoverable transformation strains.

The present work combines a rate-independent SMA model guided by the initial work of Boyd and Lagoudas (1996) with a conventional viscoplastic model (Lemaitre and Chaboche, 1990; Chaboche, 1997; Chaboche, 2008). The viscoplastic model chosen in this work is based on a thermodynamic framework that uses displacement-like internal state variables. This is in contrast with other models like that of Arnold et al. (1996), which use force-like internal state variables. The coupled SMA–viscoplastic model is numerically implemented following a numerical scheme analogous to that first proposed for rate-independent plasticity in SMAs as discussed in the work by Hartl and Lagoudas (2009).

The organization of the paper is as follows: Section 2 presents the 3-D constitutive model, derived within a thermodynamic framework in which mathematical forms for the free energy potential and evolution equations are directly postulated. The numerical implementation of the model is presented in Section 3, while in Section 4, several numerical examples are presented and discussed, including the experimental calibration of the model followed by the predictive analysis of complex SMA and HTSMA structures experiencing large deformations. The conclusions of this work are summarized in the final section.

2. Development of the constitutive model

The model derived in this work considers two distinct dissipative processes: the martensitic phase transformation and rate-dependent viscoplastic creep (or relaxation). Regarding the phase transformation, we consider both the recoverable and irrecoverable deformations resulting from this process. While the recoverable strain forms the basis for the unique shape memory behaviors observed in SMAs, the transformation-induced irrecoverable (TRIP) strain also becomes prominent in HTSMAs, where high temperatures serve to exacerbate these effects (Kumar and Lagoudas, 2007). Regarding viscoplasticity, we consider the rate-dependent evolution of an additional inelastic irrecoverable strain. This effect is not observed in conventional SMAs at conventional temperatures; it is observed when these materials are subjected to high temperatures (during processing or shape-setting). Further, these strains can be generated during the thermally induced actuation of HTSMA bodies due to the high temperatures needed to initiate transformation.

2.1. Free energy potential and thermodynamics

The derivation of the current constitutive model for a shape memory alloy undergoing viscoplastic deformations is based on considering the evolution of internal variables (scalar and tensorial) subject to the constraints of thermodynamics. To that end, we first propose:

Assumption 1. The state of the material is described by a Gibbs free energy thermodynamic potential, which is decomposed into an austenitic, martensitic, and mixing contribution, and which is dependent on particular external and internal state variables.

The Gibbs free energy potential, G, must be able to capture the thermomechanical mechanisms, both reversible and irreversible, that phenomenologically describe the material response. In order to achieve this goal, the potential G must be expressed in terms of appropriately chosen state variables. Since the transformation behavior of the material is stress and temperature dependent, the externally applied state variables are selected to be the *stress tensor* $\boldsymbol{\sigma}$ and the *absolute temperature* T. The internally evolving state variables are divided in two categories, the transformation internal state variables and the viscoplastic internal state variables. The transformation mechanisms discussed herein follow from past works found in the literature. Phase transformation is sufficiently described given knowledge of the fully recoverable *transformation strain tensor* $\boldsymbol{\varepsilon}^{\mathrm{t}}$ (Boyd and Lagoudas, 1996), the irrecoverable *TRIP strain tensor* $\boldsymbol{\varepsilon}^{\mathrm{tp}}$ (Lagoudas and Entchev, 2004), the *martensitic volume fraction* ξ (constrained such that $0 \leqslant \xi \leqslant 1$), and the *transformation hardening energy* g^{t}, which measures the change in the free energy due to transformation hardening (Machado et al., submitted for publication). On the other hand, the viscoplastic mechanisms considered have not been previously addressed in the context of shape memory alloys. The effects of viscoplasticity are characterized by the *viscoplastic strain tensor* $\boldsymbol{\varepsilon}^{\mathrm{vp}}$, and the *viscoplastic hardening energy* g^{vp}, which measures the increase in the free energy due to isotropic hardening. The introduction of hardening energy terms in the free energy potential is used in the literature (for instance, Lemaitre and Chaboche, 1990) in order to account for energy due to inelastic mechanisms that is stored inside the material and is not dissipated as heat. The proposed Gibbs free energy potential, dependent on each of these state variables, is decomposed into three contributions and written as

$$G(\boldsymbol{\sigma}, T, \boldsymbol{\varepsilon}^{\mathrm{t}}, \boldsymbol{\varepsilon}^{\mathrm{tp}}, \xi, g^{\mathrm{t}}, \boldsymbol{\varepsilon}^{\mathrm{vp}}, g^{\mathrm{vp}}) = (1-\xi)G^{\mathrm{A}}(\boldsymbol{\sigma}, T, \boldsymbol{\varepsilon}^{\mathrm{vp}}, g^{\mathrm{vp}}) + \xi G^{\mathrm{M}}(\boldsymbol{\sigma}, T, \boldsymbol{\varepsilon}^{\mathrm{vp}}, g^{\mathrm{vp}}) + G^{\mathrm{mix}}(\boldsymbol{\sigma}, \boldsymbol{\varepsilon}^{\mathrm{t}}, \boldsymbol{\varepsilon}^{\mathrm{tp}}, g^{\mathrm{t}}), \tag{2.1}$$

where[1]

$$G^{\gamma}(\boldsymbol{\sigma}, T, \boldsymbol{\varepsilon}^{\mathrm{vp}}, g^{\mathrm{vp}}) = -\frac{1}{2\rho}\boldsymbol{\sigma} : \mathscr{S}^{\gamma}\boldsymbol{\sigma} - \frac{1}{\rho}\boldsymbol{\sigma} : \boldsymbol{\varepsilon}^{\mathrm{vp}} + \frac{1}{\rho}g^{\mathrm{vp}} - \frac{1}{\rho}\boldsymbol{\sigma} : \boldsymbol{\alpha}(T - T_0) + c\left[(T - T_0) - T\ln\left(\frac{T}{T_0}\right)\right] - s_0^{\gamma}T + u_0^{\gamma} \tag{2.2}$$

for γ = A, M. Each G^{γ} represents the Gibbs energy of a conventional viscoplastic material (e.g., viscoplastic austenite). The process of transformation from one pure phase to the other is accounted for by the form of (2.1) and the energy of mixing, which includes the contributions of the transformation-induced strains (recoverable and irrecoverable); it is given as:

---

[1] The notation $(\cdot{:}\cdot)$ denotes the inner product between two second-order tensors. The product between a fourth-order tensor and a second-order tensor is represented without any such symbol (cf. Gurtin, 1981).

$$G^{\text{mix}}(\boldsymbol{\sigma},\boldsymbol{\varepsilon}^{\text{t}},\boldsymbol{\varepsilon}^{\text{tp}},g^{\text{t}}) = -\frac{1}{\rho}\boldsymbol{\sigma} : (\boldsymbol{\varepsilon}^{\text{t}}+\boldsymbol{\varepsilon}^{\text{tp}}) + \frac{1}{\rho}g^{\text{t}}. \tag{2.3}$$

The material constants $\mathscr{S}$, s_0 and u_0 denote the fourth-order compliance tensor, the specific entropy at the reference state, and the specific internal energy at the reference state, respectively, and are assumed to be different for each phase. On the other hand, $\boldsymbol{\alpha}$, ρ, and c denote the thermal expansion coefficient tensor, the density, and the specific heat, respectively, and are assumed to be invariant during phase change.

Application of the first and second laws of thermodynamics and consideration of the Legendre transformations (Lagoudas, 2008) leads to the following expression for the strong form of the second thermodynamic law:

$$-\rho\dot{G} - \dot{\boldsymbol{\sigma}} : \boldsymbol{\varepsilon} - \rho s\dot{T} \geqslant 0. \tag{2.4}$$

Using the classical procedure of Coleman and Noll (Coleman et al., 1967), we then obtain the following relations for the total infinitesimal strain and entropy:

$$\boldsymbol{\varepsilon} = \mathscr{S}\boldsymbol{\sigma} + \boldsymbol{\alpha}(T-T_0) + \boldsymbol{\varepsilon}^{\text{t}} + \boldsymbol{\varepsilon}^{\text{tp}} + \boldsymbol{\varepsilon}^{\text{vp}}, \tag{2.5}$$

$$s = \frac{1}{\rho}\boldsymbol{\sigma} : \boldsymbol{\alpha} + c\ln\left(\frac{T}{T_0}\right) + s_0. \tag{2.6}$$

Rewriting (2.5) in terms of stress and introducing $\mathscr{C} = \mathscr{S}^{-1}$, we arrive at the common form of Hooke's law, which will be useful during implementation:

$$\boldsymbol{\sigma} = \mathscr{C}\left[\boldsymbol{\varepsilon} - \boldsymbol{\alpha}(T-T_0) - \boldsymbol{\varepsilon}^{\text{t}} - \boldsymbol{\varepsilon}^{\text{tp}} - \boldsymbol{\varepsilon}^{\text{vp}}\right] = \mathscr{C}\left[\boldsymbol{\varepsilon} - \boldsymbol{\varepsilon}^{th} - \boldsymbol{\varepsilon}^{\text{t}} - \boldsymbol{\varepsilon}^{\text{tp}} - \boldsymbol{\varepsilon}^{\text{vp}}\right]. \tag{2.7}$$

Due to the decomposition of G into an austenitic and martensitic component, the material constants $\mathscr{S}$ and s_0 involved in the definition of strain and entropy are now defined in terms of the martensitic volume fraction ξ by the rule of mixtures (e.g., $\mathscr{S}(\xi) := \mathscr{S}^{\text{A}} + \xi\widetilde{\mathscr{S}}$, etc.).[2] The remaining dissipative terms resulting from application of the second law given by (2.4) consist of the partial derivatives of G with respect to each independent internal variable. Separated into transformation and viscoplastic contributions, this is written[3]

$$\begin{aligned}
&-\rho\left[\partial_{\xi}G\dot{\xi} + \partial_{\boldsymbol{\varepsilon}^{\text{t}}}G^{\text{mix}} : \dot{\boldsymbol{\varepsilon}}^{\text{t}} + \partial_{\boldsymbol{\varepsilon}^{\text{tp}}}G^{\text{mix}} : \dot{\boldsymbol{\varepsilon}}^{\text{tp}} + \partial_{g^{\text{t}}}G^{\text{mix}}\dot{g}^{\text{t}}\right] \\
&-\rho\left[(1-\xi)\partial_{\boldsymbol{\varepsilon}^{\text{vp}}}G^{\text{A}} + \xi\partial_{\boldsymbol{\varepsilon}^{vp}}G^{\text{M}}\right] : \dot{\boldsymbol{\varepsilon}}^{\text{vp}} - \rho\left[(1-\xi)\partial_{g^{\text{vp}}}G^{\text{A}} + \xi\partial_{g^{\text{vp}}}G^{\text{M}}\right]\dot{g}^{\text{vp}} \geqslant 0.
\end{aligned} \tag{2.8}$$

2.2. Evolution of internal variables

Assumption 2. The rate of evolution of the transformation-induced strains is proportional to the rate of the martensitic volume fraction, $\dot{\xi}$, and this rate alone. Likewise, the rate of evolution of the viscoplastic strain is proportional to the rate of the effective viscoplastic strain, $\dot{p}$, and this rate alone.

Using the form employed in various transformation and transformation–plastic models (Boyd and Lagoudas, 1996; Lagoudas and Entchev, 2004), the 3-D evolutions of the transformation, TRIP, and viscoplastic strains are given as

$$\dot{\boldsymbol{\varepsilon}}^{\text{t}} = \dot{\xi}\boldsymbol{\Lambda}^{\text{t}}; \qquad \dot{\boldsymbol{\varepsilon}}^{\text{tp}} = \dot{\xi}\boldsymbol{\Lambda}^{\text{tp}}; \qquad \dot{\boldsymbol{\varepsilon}}^{\text{vp}} = \dot{p}\boldsymbol{\Lambda}^{\text{vp}}. \tag{2.9}$$

It is assumed that evolution of the transformation strain results only from evolution of the total martensitic volume fraction (i.e., occurs only during phase transformation). Possible evolution in the recoverable inelastic strain resulting from martensitic reorientation is not accounted for. Therefore, the model is not intended for the analysis of strongly non-proportional loading paths sufficient to induce the reorientation of martensite already formed. The scalar p denotes the *effective viscoplastic strain*, whose rate is given from the second invariant of the viscoplastic strain rate per $\dot{p} = \sqrt{2/3(\dot{\boldsymbol{\varepsilon}}^{\text{vp}} : \dot{\boldsymbol{\varepsilon}}^{\text{vp}})}$. The directions of the evolutions are given as

$$\begin{aligned}
&\boldsymbol{\Lambda}^{\text{t}} = \begin{cases} H^{\text{cur}}(\bar{\sigma})\frac{3}{2}\frac{\boldsymbol{\sigma}'}{\bar{\sigma}}; & \dot{\xi} > 0 \\ \frac{\boldsymbol{\varepsilon}^{t-r}}{\xi^{r}}; & \dot{\xi} < 0 \end{cases}; \qquad \boldsymbol{\Lambda}^{\text{tp}} = \begin{cases} f^{\text{tp}}(\bar{\sigma})\boldsymbol{\Lambda}^{\text{vp}}; & \dot{\xi} > 0 \\ -f^{\text{tp}}(\bar{\sigma})\boldsymbol{\Lambda}^{\text{vp}}; & \dot{\xi} < 0 \end{cases}; \\
&\boldsymbol{\Lambda}^{\text{vp}} = \frac{3}{2}\frac{\boldsymbol{\sigma}'}{\bar{\sigma}}.
\end{aligned} \tag{2.10}$$

During forward transformation $\left(\dot{\xi} > 0\right)$, the transformation strain is clearly generated in the direction of the deviatoric stress $\boldsymbol{\sigma}'$, which is normalized by the *Mises equivalent stress* $\bar{\sigma} = \sqrt{(3/2\boldsymbol{\sigma}' : \boldsymbol{\sigma}')}$. This direction, which has a norm of unity, is also used

---

[2] Throughout this work we will adopt the notation that, for any quantity x defined in the pure austenitic phase (x^{A}) and pure martensitic phase (x^{M}), the difference is given as $\tilde{x} = x^{\text{M}} - x^{\text{A}}$. The use of the symbol Δ, commonly applied for this purpose, is reserved for Section 3.

[3] For partial derivatives, a shortened notation is used such that $\partial_x = \frac{\partial}{\partial x}$.

for the evolution of TRIP and viscoplastic strains, and is the standard plastic strain direction tensor normal to the classical Mises plastic yield function (in stress space) (Khan and Huang, 1995). The magnitude of the transformation strain generated during full forward transformation is given by $H^{\mathrm{cur}}(\bar{\sigma})$ (specified shortly), while the scalar-valued function $f^{\mathrm{tp}}(\bar{\sigma})$ describes the magnitude of the TRIP strain generation rate at a given stress, and is calibrated from experimental results.[4]

During full reverse transformation $\left(\dot{\xi} < 0\right)$, the transformation strain generated during the previous forward transformation must be recovered (by definition). This motivates the form of $\boldsymbol{\Lambda}^{\mathrm{t}}$ during reverse transformation, where $\boldsymbol{\varepsilon}^{t-r}$ denotes the transformation strain at transformation reversal (i.e., the state at which the most recent *forward* transformation ended) and the scalar ξ^{r} is the martensitic volume fraction at the transformation reversal, used for renormalization.

The choice of the function $H^{\mathrm{cur}}(\bar{\sigma})$ has been discussed in detail elsewhere (Hartl et al., 2009); here we find it sufficient to state that

$$H^{\mathrm{cur}}(\bar{\sigma}) = \begin{cases} H_{\min}; & \bar{\sigma} \leqslant \bar{\sigma}_{\mathrm{crit}}, \\ H_{\min} + (H_{\max} - H_{\min})\left(1 - e^{-k(\bar{\sigma} - \bar{\sigma}_{\mathrm{crit}})}\right); & \bar{\sigma} > \bar{\sigma}_{\mathrm{crit}}, \end{cases} \tag{2.11}$$

where $H_{\min}$ corresponds to the observable uniaxial two-way shape memory effect (TWSME) while the parameter $H_{\max}$ describes the ultimate transformation strain given uniaxial loading (i.e., the maximum recoverable transformation strain generated considering all applicable stress levels). Additionally, $\bar{\sigma}_{\mathrm{crit}}$ denotes the critical Mises equivalent stress below which $H^{\mathrm{cur}}(\bar{\sigma}) = H_{\min}$, and the parameter k controls the rate at which $H^{\mathrm{cur}}(\bar{\sigma})$ exponentially evolves from $H_{\min}$ to $H_{\max}$. This parameter can be fit by minimizing the square of the error between the H^{cur} curve and the available data points, for example.

Having fully described the evolution equations for the various inelastic strains, we must postulate an evolution equation for the transformation hardening energy. The following form is chosen such that a *smooth* transition to/from transformation response is provided (Machado et al., submitted for publication):

$$\dot{g}^{\mathrm{t}} = \dot{\xi} \begin{cases} \frac{1}{2} a_1 \left(1 + \xi^{n_1} - (1 - \xi)^{n_2}\right) + a_3; & \dot{\xi} > 0 \\ \frac{1}{2} a_2 \left(1 + \xi^{n_3} - (1 - \xi)^{n_4}\right) - a_3; & \dot{\xi} < 0 \end{cases} = \dot{\xi} f^{\mathrm{t}}(\xi), \tag{2.12}$$

where the constants $a_1,\ a_2,$ and a_3 are calibrated from the SMA phase diagram (see Appendix A) and the constants $n_1 - n_4$ are given values between 0 and 1, where values near 0 provide a more gradual transition into and out of the transformation response. The proposed form of the rate of transformation hardening energy guarantees that, upon completion of a full transformation cycle, the transformation hardening energy reverts to zero. Thus, in the case of full transformation and no plastic mechanisms, the material returns to its initial energy state.

Additionally, we postulate an evolution equation for the viscoplastic hardening energy, given as

$$\dot{g}^{\mathrm{vp}} = \dot{p} f^{\mathrm{vp}}(T, p). \tag{2.13}$$

During viscoplastic deformation, the rate of increase in the viscoplastic hardening energy is proportional to the rate of the effective plastic strain by the factor $f^{\mathrm{vp}}(T, p)$, which, in general, is temperature-dependent.

2.3. Criteria for transformation and viscoplastic yield

Substituting the proposed evolution equations into the dissipative inequality (2.8), we arrive at

$$\left[\boldsymbol{\sigma} : (\boldsymbol{\Lambda}^{\mathrm{t}} + \boldsymbol{\Lambda}^{\mathrm{tp}}) - \rho \partial_{\xi} G - f^{\mathrm{t}}(\xi)\right] \dot{\xi} + [\boldsymbol{\sigma} : \boldsymbol{\Lambda}^{\mathrm{vp}} - f^{\mathrm{vp}}(T, p)] \dot{p} \geqslant 0. \tag{2.14}$$

Assumption 3. The two processes of phase transformation and viscoplasticity are independently strongly dissipative. The Clausius–Duhem inequality is decomposed into two additive contributions, each being independently strictly positive during evolution of the corresponding internal variables.

This assumption is inspired by the work of past modelers who enforced a strict inequality during dissipation (Anand and Gurtin, 2003) and further required that each bracketed term in (2.14) be independently non-negative (Germain, 1973; Boyd and Lagoudas, 1996). This is clearly a sufficient condition to ensure that the total inequality will also be satisfied. This assumption leads to the following set of two conditions:

$$\begin{aligned} &[\boldsymbol{\sigma} : (\boldsymbol{\Lambda}^{\mathrm{t}} + \boldsymbol{\Lambda}^{\mathrm{tp}}) - \rho \partial_{\xi} G - f^{\mathrm{t}}(\xi)] \dot{\xi} = \pi^{\mathrm{t}} \dot{\xi} > 0 \quad \forall \dot{\xi} \neq 0, \\ &[\boldsymbol{\sigma} : \boldsymbol{\Lambda}^{\mathrm{vp}} - f^{\mathrm{vp}}(T, p)] \dot{p} = \pi^{\mathrm{vp}} \dot{p} > 0 \quad \forall \dot{p} > 0. \end{aligned} \tag{2.15}$$

From $(2.15)_1$ it follows that π^{t} must be non-zero whenever ξ is evolving, and further, that π^{t} must change sign as $\dot{\xi}$ changes sign. Considering these constraints and postulating a limit value for π^{t} during transformation, we arrive at the consistency (or Kuhn–Tucker) conditions on transformation, given as

---

[4] Note that in past works (i.e., Lagoudas and Entchev, 2004), the TRIP strain was postulated to stabilize and its evolution cease as the number of transformation cycles increased. This stabilization is not considered in the present work as the high temperatures experienced by HTSMAs during transformation can annihilate dislocations in each cycle, resulting in a constant (non-decreasing) rate of TRIP strain generation (Kumar and Lagoudas, 2007).

$$\Phi^{\mathrm{t}} \leqslant 0; \quad \dot{\xi}\Phi^{\mathrm{t}} = 0, \tag{2.16}$$

where, in the case that $\dot{\xi} \geqslant 0$ and $0 \leqslant \xi < 1$, we have

$$\Phi^{\mathrm{t}} = \Phi^{t(+)} = \pi^{\mathrm{t}} - Y^{\mathrm{t}}(\boldsymbol{\sigma}),$$

while, in the case of $\dot{\xi} \leqslant 0$ and $0 < \xi \leqslant 1$, we have

$$\Phi^{\mathrm{t}} = \Phi^{t(-)} = -\pi^{\mathrm{t}} - Y^{\mathrm{t}}(\boldsymbol{\sigma}).$$

During elastic loading of a mixed phase $\left(\dot{\xi} = 0 \text{ and } 0 < \xi < 1\right)$, both cases may exist simultaneously, and thus both $\Phi^{t(+)} \leqslant 0$ and $\Phi^{t(-)} \leqslant 0$ must be maintained. It can be seen that

$$\pi^{\mathrm{t}} = \boldsymbol{\sigma} : \left(\boldsymbol{\Lambda}^{\mathrm{t}} + \boldsymbol{\Lambda}^{\mathrm{tp}}\right) + \frac{1}{2}\boldsymbol{\sigma} : \widetilde{\mathscr{S}}\boldsymbol{\sigma} + \rho\tilde{s}_0 T - \rho\tilde{u}_0 - f^{\mathrm{t}}(\xi), \tag{2.17}$$

and the parameters $\rho\tilde{s}_0$ and $\rho\tilde{u}_0$ and function $Y^{\mathrm{t}}(\boldsymbol{\sigma})$ are directly calibrated from parameters describing the SMA phase diagram as summarized in Appendix A.

Similarly, constraints on the evolution of $\boldsymbol{\varepsilon}^{\mathrm{vp}}$ (and thus p) result from $(2.15)_2$. In rate-independent classical plasticity, these are satisfied by a plastic consistency condition similar to (2.16). In the current model, however, we satisfy $(2.15)_2$ by explicitly postulating a functional form for p as motivated by the work of Lemaitre and Chaboche (1990) and Chaboche (2008). This form is assumed valid for isotropic viscoplastic hardening and considers both primary and secondary creep. It guarantees positive dissipation and the satisfaction of the second law (2.15). The evolution of effective viscoplastic strain is then given as

$$\dot{p} = \lambda^{\mathrm{vp}}(\boldsymbol{\sigma}, T, p) = \left(\frac{\langle \boldsymbol{\sigma} : \boldsymbol{\Lambda}^{\mathrm{vp}} - f^{\mathrm{vp}}(T, p)\rangle}{K_{\mathrm{a}}(T)}\right)^{N_{\mathrm{a}}(T)}, \tag{2.18}$$

where K_{a} and N_{a} are generally temperature-dependent functions and $\langle\cdot\rangle$ denote the Macaulay brackets.[5] In the special case that one considers only small thermal excursions from the reference state, the explicit dependence of N_{a} on temperature can be neglected.

The thermally activated processes that underlie creep can be sufficiently captured using the Arrhenius' equation. Further, if the critical stress for creep is sufficiently small (i.e., $f^{\mathrm{vp}}(T, p) \approx 0$), the empirical Norton's law in its 3-D form (see Odqvist, 1966) can be used to address the stress-dependence of viscoplastic strain evolution. Given these assumptions and further noting that $\boldsymbol{\sigma} : \boldsymbol{\Lambda}^{\mathrm{vp}} \geqslant 0$, making the Macaulay brackets unnecessary, the form of λ^{vp} can be reduced to

$$\lambda^{\mathrm{vp}}(\boldsymbol{\sigma}, T) = A\exp\left(\frac{-Q}{RT}\right)(\boldsymbol{\sigma} : \boldsymbol{\Lambda}^{\mathrm{vp}})^{N_{\mathrm{a}}}, \tag{2.19}$$

where Q is the activation energy, R is the gas constant, and A is an additional fitting parameter. Combining (2.18) and (2.19), we find

$$K_{\mathrm{a}}(T) = \left[A\exp\left(\frac{-Q}{RT}\right)\right]^{-1/N_{\mathrm{a}}}. \tag{2.20}$$

2.4. Summary of the constitutive model equations

To summarize the various essential relations for capturing the thermomechanical behavior of an SMA material experiencing viscoplastic deformation using the model above, Table 1 is provided. These relations apply at any given material point provided that the temperature is known locally. The calibration of the various model parameters is discussed in Appendix A. Considering the model equations presented in this chapter, the calibration discussion in that appendix, and assuming a quadratic form for the function f^{tp}, the total number of material parameters is found to be at most 25. Specifically, we have:[6]

- Five thermoelastic properties (two elastic constants for each phase and one common coefficient of thermal expansion).
- Four properties to describe $H^{\mathrm{cur}}(\bar{\sigma})$.
- Four transformation temperatures.
- Two stress influence coefficients (the slopes of the transformation surfaces in the phase diagram).
- Four hardening coefficients n_1–n_4.
- Three coefficients for a quadratic $f^{\mathrm{tp}}(\bar{\sigma})$.
- Three viscoplastic parameters (A, Q, and N_{a}).

---

[5] The Macauley brackets are defined such that $\langle x\rangle = \begin{cases} x; & x \geqslant 0 \\ 0; & x < 0 \end{cases} = \frac{x+|x|}{2}$.

[6] These 24 can each be seen in Table 3 provided in the discussion of Section 4.1.

Table 1
Summary of SMA transformation–viscoplastic model equations.

Total strain

$$\boldsymbol{\varepsilon} = \mathscr{S}\boldsymbol{\sigma} + \boldsymbol{\alpha}(T - T_0) + \boldsymbol{\varepsilon}^{\mathrm{t}} + \boldsymbol{\varepsilon}^{\mathrm{tp}} + \boldsymbol{\varepsilon}^{\mathrm{vp}}$$

Evolution equations of inelastic strains

$$\dot{\boldsymbol{\varepsilon}}^{\mathrm{t}} = \dot{\xi}\begin{cases} H^{\mathrm{cur}}(\bar{\sigma})\frac{3}{2}\frac{\boldsymbol{\sigma}'}{\bar{\sigma}}; & \dot{\xi} > 0 \\ \frac{\boldsymbol{\varepsilon}^{t-r}}{\xi^{r}}; & \dot{\xi} < 0 \end{cases}$$

$$\dot{\boldsymbol{\varepsilon}}^{\mathrm{tp}} = |\dot{\xi}| f^{\mathrm{tp}}(\bar{\sigma})\frac{3}{2}\frac{\boldsymbol{\sigma}'}{\bar{\sigma}}$$

$$\dot{\boldsymbol{\varepsilon}}^{\mathrm{vp}} = \dot{p}\frac{3}{2}\frac{\boldsymbol{\sigma}'}{\bar{\sigma}}$$

Evolution of martensitic volume fraction

$$\Phi^{t(+)} = (1 - D)\left(H^{\mathrm{cur}}(\bar{\sigma})\bar{\sigma} + f^{\mathrm{tp}}(\bar{\sigma})\bar{\sigma}\right) + \frac{1}{2}\boldsymbol{\sigma} : \widetilde{\mathscr{S}}\boldsymbol{\sigma} + \rho\tilde{s}_0 T - \rho\tilde{u}_0 - \left(\frac{1}{2}a_1\left(1 + \xi^{n_1} - (1 - \xi)^{n_2}\right) + a_3\right) - Y_0^{\mathrm{t}}$$

$$\Phi^{t(-)} = -(1 + D)\left(\frac{\boldsymbol{\sigma} : \boldsymbol{\varepsilon}^{t-r}}{\xi^{r}} - f^{\mathrm{tp}}(\bar{\sigma})\bar{\sigma}\right) - \frac{1}{2}\boldsymbol{\sigma} : \widetilde{\mathscr{S}}\boldsymbol{\sigma} - \rho\tilde{s}_0 T + \rho\tilde{u}_0 + \left(\frac{1}{2}a_2\left(1 + \xi^{n_3} - (1 - \xi)^{n_4}\right) - a_3\right) - Y_0^{\mathrm{t}}$$

$$\Phi^{\mathrm{t}} = \begin{cases} \Phi^{t(+)}; & \dot{\xi} \geqslant 0 \text{ and } 0 \leqslant \xi < 1 \\ \Phi^{t(-)}; & \dot{\xi} \leqslant 0 \text{ and } 0 < \xi \leqslant 1 \end{cases}$$

$$\Phi^{\mathrm{t}} \leqslant 0, \quad \dot{\xi}\Phi^{\mathrm{t}} = 0, \quad 0 \leqslant \xi \leqslant 1$$

Evolution of effective viscoplastic strain

$$\dot{p} = A\exp\left(\frac{-Q}{RT}\right)\bar{\sigma}^{N_a}$$

This number can be reduced to 16 if the elastic properties of the two phases are assumed equal, the maximum transformation strain H^{cur} is taken to be constant, one stress influence coefficient is used, and the hardening during transformation is described by a single parameter (e.g., for linear hardening $n_1 = n_2 = n_3 = n_4 = 1$).

3. Numerical implementation

The purpose behind developing constitutive models for SMAs and HTSMAs is to solve boundary value problems and predict the thermomechanical behavior of structural components composed of these materials. To this end, the mathematical model of Section 2 must be implemented numerically; a discussion of this follows. The methodology is inspired by and follows closely from other developments in the literatures (Qidwai and Lagoudas, 2000; Hartl and Lagoudas, 2009), but the simultaneous evolution in three inelastic strains necessitates the consideration of new complexities.

To analyze 3-D structural response, the model is implemented within an established FEA framework seeking to find the global force equilibrium solution. The material behavior at each local material (integration) point in each element sub-domain is defined by the constitutive relations of Section 2. In solving problems that present non-linearities (e.g., material or geometric), the time history of any defined force or displacement applied in the FEA is partitioned into increments, or *loading steps*. During each step of this incremental solution process, the global FEA solver attempts to satisfy the balance of equilibrium in the global sense by determining appropriate increments of total strain and temperature locally for each integration point of each element using an iterative method (e.g., Newton–Raphson) (Reddy, 2004). Given these two local inputs $\{\boldsymbol{\varepsilon}, T\}$, the SMA constitutive model, numerically implemented in the form of a *user material subroutine*, is used to calculate the local stress and internal variable increments, which are returned to the global solver. Also calculated is the local tangent stiffness tensor, which is necessary for convergence of the global Newton–Raphson algorithm.

3.1. Integration of the coupled phase transformation–viscoplastic evolution equations

The task of the user material subroutine for the current model is the simultaneous and coupled integration of the evolution equations for both viscoplastic and transformation-related strains. Different implementation methodologies exist, and several of these are discussed in detail for the special case of viscoplastic deformation only (no phase transformation) in Appendix B. Each of the methods described there could be extended to the simultaneous case, and here we consider one: the *convex cutting plane* form of the return mapping algorithm (RMA) (Ortiz and Simo, 1986). Such was the method described for the integration of the phase transformation relations in the work by Qidwai and Lagoudas (2000), and the same notation is used in the present work.[7]

To begin, we rewrite (2.7) in the incremental-iterative form such that the stress during the current loading increment $n+1$ at the end of each iteration k is given as

$$\boldsymbol{\sigma}^{(k)}_{n+1} = \mathscr{C}^{(k)}_{n+1}\left[\boldsymbol{\varepsilon}_{n+1} - \boldsymbol{\varepsilon}^{th}_{n+1} - \boldsymbol{\varepsilon}^{t(k)}_{n+1} - \boldsymbol{\varepsilon}^{\mathrm{tp}(k)}_{n+1} - \boldsymbol{\varepsilon}^{\mathrm{vp}(k)}_{n+1}\right]. \tag{3.1}$$

Recall that for each loading step, the total strain increment and temperature increment are supplied by the global solver and are thus known. It is the role of the user material subroutine to find the current stress, which may require the integration of the evolution equations for $\boldsymbol{\varepsilon}^{\mathrm{t}}$, $\boldsymbol{\varepsilon}^{\mathrm{tp}}$, and $\boldsymbol{\varepsilon}^{\mathrm{vp}}$. The overall process of finding $\boldsymbol{\sigma}$ can be performed using a predictor-corrector scheme where, for each loading step, purely thermoelastic relations are first used to calculate a possible solution based on the assumption that the inelastic strains are not evolving (a prediction). Specifically,

$$\boldsymbol{\varepsilon}^{t(0)}_{n+1} = \boldsymbol{\varepsilon}^{\mathrm{t}}_{n}, \qquad \boldsymbol{\varepsilon}^{\mathrm{tp}(0)}_{n+1} = \boldsymbol{\varepsilon}^{\mathrm{tp}}_{n}, \qquad \boldsymbol{\varepsilon}^{\mathrm{vp}(0)}_{n+1} = \boldsymbol{\varepsilon}^{\mathrm{vp}}_{n}, \qquad p^{(0)}_{n+1} = p_n. \tag{3.2}$$

The transformation function (2.16) and viscoplastic strain rate (2.18) are then calculated based on this prediction. If the transformation criteria are not violated (i.e., if $\Phi^{t(0)}_{n+1} \leqslant 0$) and if the effective strain rate (2.18) is null, the elastic solution is accepted as correct and is returned to the global solver. However, if one or both of these functions Φ^{t} or λ^{vp} is found to have a positive value based on the prediction (3.2), evolution of the applicable inelastic internal variables via the return mapping algorithm is applied (a correction). The iterative correction process completes when Φ^{t} is sufficiently close to zero and $\dot{p}$ is sufficiently close to the value of the evaluated function λ^{vp}.

During iterative correction, we recall that the total current strain $\boldsymbol{\varepsilon}_{n+1}$ and current temperature T_{n+1} (i.e., at time t_{n+1}) are given. The solutions for the inelastic strains are updated using the following for the transformation and viscoplastic strains (cf. (2.9)):

$$\begin{aligned}
\boldsymbol{\varepsilon}^{\mathrm{tp}(k+1)}_{n+1} &= \boldsymbol{\varepsilon}^{\mathrm{tp}}_{n} + \left(\xi^{(k+1)}_{n+1} - \xi_n\right)\boldsymbol{\Lambda}^{\mathrm{tp}}\left(\boldsymbol{\sigma}^{(k)}_{n+1}\right),\\
\boldsymbol{\varepsilon}^{t(k+1)}_{n+1} &= \boldsymbol{\varepsilon}^{\mathrm{t}}_{n} + \left(\xi^{(k+1)}_{n+1} - \xi_n\right)\boldsymbol{\Lambda}^{\mathrm{t}}\left(\boldsymbol{\sigma}^{(k)}_{n+1}\right),\\
\boldsymbol{\varepsilon}^{\mathrm{vp}(k+1)}_{n+1} &= \boldsymbol{\varepsilon}^{\mathrm{vp}}_{n} + \Delta t\dot{p}^{(k+1)}_{n+1}\boldsymbol{\Lambda}^{\mathrm{vp}}\left(\boldsymbol{\sigma}^{(k)}_{n+1}\right).
\end{aligned} \tag{3.3}$$

The scalar-valued internal variables upon which the convex cutting plane algorithm is based are iteratively written as

$$\xi^{(k+1)}_{n+1} = \xi^{(k)}_{n+1} + \Delta\xi^{(k)}_{n+1}, \qquad \dot{p}^{(k+1)}_{n+1} = \dot{p}^{(k)}_{n+1} + \Delta\dot{p}^{(k)}_{n+1}, \tag{3.4}$$

where we now seek the unknowns $\Delta\xi^{(k)}_{n+1}$ and $\Delta\dot{p}^{(k)}_{n+1}$.

It can be shown using (2.16), (3.1), (3.3) and (3.4) (see Qidwai and Lagoudas, 2000) that the iterative change in stress during correction is[8]

$$\Delta\boldsymbol{\sigma}^{(k)}_{n+1} = \mathscr{C}^{(k)}_{n+1}\left[\mp\left(\partial_{\boldsymbol{\sigma}}\Phi^{t(k)}_{n+1} + D\left(\boldsymbol{\Lambda}^{t(k)}_{n+1} + \boldsymbol{\Lambda}^{\mathrm{tp}(k)}_{n+1}\right)\right)\Delta\xi^{(k)}_{n+1} - \boldsymbol{\Lambda}^{\mathrm{vp}(k)}_{n+1}\Delta\dot{p}^{(k)}_{n+1}\Delta t\right], \tag{3.5}$$

where the "$\mp$" corresponds to forward/reverse transformation, respectively.

Here we introduce a constraint equation for the value of $\dot{p}$ analogous to Φ^{t}. Using (2.18), we form

$$\Phi^{\mathrm{vp}}(\boldsymbol{\sigma}, T, p, \dot{p}) = \lambda^{\mathrm{vp}}(\boldsymbol{\sigma}, T, p) - \dot{p} = 0, \tag{3.6}$$

where this is discussed further in Appendix B. Linearizing the transformation function $\Phi^{\mathrm{t}}(\boldsymbol{\sigma}, T, \xi)$ and this new viscoplastic strain rate constraint equation $\Phi^{\mathrm{vp}}(\boldsymbol{\sigma}, T, p, \dot{p})$ about their roots, we have

---

[7] The notation is as follows: given any quantity x, its value is updated from the previous time step to the current in the backward Euler sense per $x_{n+1} = x_n + \Delta x_{n+1}$. Such an implicit relation is solved iteratively, and the current value is updated from iteration to iteration per $x^{(k+1)}_{n+1} = x^{(k)}_{n+1} + \Delta x^{(k)}_{n+1}$ until x_{n+1} has converged (see Appendix B).

[8] The parameter D results from the proposed functional form for $Y^{\mathrm{t}}(\boldsymbol{\sigma})$ (see (2.16)). It is zero-valued if the slopes of the forward and reverse transformation surfaces in the phase diagram (σ–T space) are equivalent and there is no evolution of TRIP strain (see Appendix A).

$$\varPhi^{t(k+1)}_{n+1} = \varPhi^{t(k)}_{n+1} + \Delta\varPhi^{t(k)}_{n+1} \simeq 0, \quad \varPhi^{\mathrm{vp}(k+1)}_{n+1} = \varPhi^{\mathrm{vp}(k)}_{n+1} + \Delta\varPhi^{\mathrm{vp}(k)}_{n+1} \simeq 0. \tag{3.7}$$

Application of the chain rule to these two relations implies

$$\varPhi^{t(k)}_{n+1} + \partial_{\boldsymbol{\sigma}}\varPhi^{t(k)}_{n+1} : \Delta\boldsymbol{\sigma}^{(k)}_{n+1} + \partial_{\xi}\varPhi^{t(k)}_{n+1}\Delta\xi^{(k)}_{n+1} \simeq 0, \tag{3.8}$$

$$\varPhi^{\mathrm{vp}(k)}_{n+1} + \partial_{\boldsymbol{\sigma}}\varPhi^{\mathrm{vp}(k)}_{n+1} : \Delta\boldsymbol{\sigma}^{(k)}_{n+1} + \partial_{p}\varPhi^{\mathrm{vp}(k)}_{n+1}\Delta p^{(k)}_{n+1} + \partial_{\dot{p}}\varPhi^{(vpk)}_{n+1}\Delta\dot{p}^{(k)}_{n+1} \simeq 0, \tag{3.9}$$

where we note that $\Delta p^{(k)}_{n+1} = \Delta\dot{p}^{(k)}_{n+1}\Delta t$ for a specified constant time increment Δt. Substituting the stress increment (3.5) into (3.8), we find

$$\varPhi^{t(k)}_{n+1} - \partial_{\boldsymbol{\sigma}}\varPhi^{t(k)}_{n+1} : \mathscr{C}^{(k)}_{n+1}\left[\pm\left(\partial_{\boldsymbol{\sigma}}\varPhi^{t(k)}_{n+1} + D\left(\boldsymbol{\Lambda}^{t(k)}_{n+1} + \boldsymbol{\Lambda}^{\mathrm{tp}(k)}_{n+1}\right)\right)\Delta\xi^{(k)}_{n+1} + \boldsymbol{\Lambda}^{\mathrm{vp}(k)}_{n+1}\Delta t\Delta\dot{p}^{(k)}_{n+1}\right] + \partial_{\xi}\varPhi^{t(k)}_{n+1}\Delta\xi^{(k)}_{n+1} \simeq 0. \tag{3.10}$$

Likewise, substituting the stress increment (3.5) into (3.9) while further considering (3.6), we find

$$\varPhi^{\mathrm{vp}(k)}_{n+1} - \partial_{\boldsymbol{\sigma}}\lambda^{\mathrm{vp}(k)}_{n+1} : \mathscr{C}^{(k)}_{n+1}\left[\pm\left(\partial_{\boldsymbol{\sigma}}\varPhi^{t(k)}_{n+1} + D\left(\boldsymbol{\Lambda}^{t(k)}_{n+1} + \boldsymbol{\Lambda}^{\mathrm{tp}(k)}_{n+1}\right)\right)\Delta\xi^{(k)}_{n+1} + \boldsymbol{\Lambda}^{\mathrm{vp}(k)}_{n+1}\Delta t\Delta\dot{p}^{(k)}_{n+1}\right] + \left[\partial_{p}\lambda^{\mathrm{vp}(k)}_{n+1}\Delta t - 1\right]\Delta\dot{p}^{(k)}_{n+1} \simeq 0. \tag{3.11}$$

Solving (3.10) for the correction in ξ at the given iteration yields

$$\Delta\xi^{(k)}_{n+1} = \frac{-\varPhi^{t(k)}_{n+1} + A^{\mathrm{t}}_{1}\Delta\dot{p}^{(k)}_{n+1}}{A^{\mathrm{t}}_{2}}, \tag{3.12}$$

where

$$\begin{aligned} A^{\mathrm{t}}_{1} &= \partial_{\boldsymbol{\sigma}}\varPhi^{t(k)}_{n+1} : \mathscr{C}^{(k)}_{n+1}\boldsymbol{\Lambda}^{\mathrm{vp}(k)}_{n+1}\Delta t; \\ A^{\mathrm{t}}_{2} &= \partial_{\xi}\varPhi^{t(k)}_{n+1} \mp \partial_{\boldsymbol{\sigma}}\varPhi^{t(k)}_{n+1} : \mathscr{C}^{(k)}_{n+1}\left(\partial_{\boldsymbol{\sigma}}\varPhi^{t(k)}_{n+1} + D\left(\boldsymbol{\Lambda}^{t(k)}_{n+1} + \boldsymbol{\Lambda}^{\mathrm{tp}(k)}_{n+1}\right)\right). \end{aligned} \tag{3.13}$$

Note that if viscoplastic yield is not occurring ($\lambda^{\mathrm{vp}} = 0$), Eq. (3.12) with $\Delta\dot{p}^{(k)}_{n+1} = \dot{p}^{(k)}_{n+1} = 0$ is used to apply the RMA to the evolution of $\{\xi, \boldsymbol{\varepsilon}^{\mathrm{t}}, \boldsymbol{\varepsilon}^{\mathrm{tp}}\}$ while $\{\dot{p}, p, \boldsymbol{\varepsilon}^{\mathrm{vp}}\}$ remain constant. Likewise rearranging (3.11) to find the viscoplastic increment gives

$$\Delta\dot{p}^{(k)}_{n+1} = \frac{-\varPhi^{\mathrm{vp}(k)}_{n+1} + A^{\mathrm{vp}}_{1}\Delta\xi^{(k)}_{n+1}}{A^{\mathrm{vp}}_{2}}, \tag{3.14}$$

where

$$\begin{aligned} A^{\mathrm{vp}}_{1} &= \pm\partial_{\boldsymbol{\sigma}}\lambda^{\mathrm{vp}(k)}_{n+1} : \mathscr{C}^{(k)}_{n+1}\left(\partial_{\boldsymbol{\sigma}}\varPhi^{t(k)}_{n+1} + D\left(\boldsymbol{\Lambda}^{t(k)}_{n+1} + \boldsymbol{\Lambda}^{\mathrm{tp}(k)}_{n+1}\right)\right); \\ A^{\mathrm{vp}}_{2} &= \partial_{p}\lambda^{\mathrm{vp}(k)}_{n+1}\Delta t - \partial_{\boldsymbol{\sigma}}\lambda^{\mathrm{vp}(k)}_{n+1} : \mathscr{C}^{(k)}_{n+1}\boldsymbol{\Lambda}^{\mathrm{vp}(k)}_{n+1}\Delta t - 1. \end{aligned} \tag{3.15}$$

The relation (3.14) with $\Delta\xi^{(k)}_{n+1} = 0$ is used directly when only viscoplastic yield is occurring $\left(\dot{\xi} = 0\right)$.

Solving the two equations (3.12) and (3.14) for the two unknowns $\Delta\xi^{(k)}_{n+1}$ and $\Delta\dot{p}^{(k)}_{n+1}$, we arrive at the final form for calculating the simultaneous inelastic corrections for the transformation and viscoplastic deformation processes. This is given for transformation as

$$\Delta\xi^{(k)}_{n+1} = \frac{-\varPhi^{t(k)}_{n+1}A^{\mathrm{vp}}_{2} - \varPhi^{\mathrm{vp}(k)}_{n+1}A^{\mathrm{t}}_{1}}{A^{\mathrm{t}}_{2}A^{\mathrm{vp}}_{2} - A^{\mathrm{t}}_{1}A^{\mathrm{vp}}_{1}}, \tag{3.16}$$

while for the viscoplastic phenomena, the corresponding correction is given as

$$\Delta\dot{p}^{(k)}_{n+1} = \frac{-\varPhi^{\mathrm{vp}(k)}_{n+1}A^{\mathrm{t}}_{2} - \varPhi^{t(k)}_{n+1}A^{\mathrm{vp}}_{1}}{A^{\mathrm{t}}_{2}A^{\mathrm{vp}}_{2} - A^{\mathrm{t}}_{1}A^{\mathrm{vp}}_{1}}. \tag{3.17}$$

It is important to recall that transformation ends when $\xi^{(k+1)}_{n+1}$ reaches one of two limits, specifically

$$0 \leqslant \xi^{(k+1)}_{n+1} \leqslant 1. \tag{3.18}$$

A given bound will always be reached during the iterative scheme within a single loading increment. Therefore, the implemented algorithm must allow a switch from (3.17) to (3.14) when $\xi^{(k)}_{n+1}$ reaches a bound, implying $\Delta\xi^{(k)}_{n+1} = 0$.

Substituting (3.4) into (3.3), it can be seen that the inelastic strains can be iteratively updated as follows:

$$\boldsymbol{\varepsilon}^{t(k+1)}_{n+1} = \boldsymbol{\varepsilon}^{t(k)}_{n+1} + \Delta\xi^{(k)}_{n+1}\boldsymbol{\Lambda}^{t(k)}_{n+1}, \quad \boldsymbol{\varepsilon}^{\mathrm{tp}(k+1)}_{n+1} = \boldsymbol{\varepsilon}^{\mathrm{tp}(k)}_{n+1} + \Delta\xi^{(k)}_{n+1}\boldsymbol{\Lambda}^{\mathrm{tp}(k)}_{n+1}, \quad \boldsymbol{\varepsilon}^{\mathrm{vp}(k+1)}_{n+1} = \boldsymbol{\varepsilon}^{\mathrm{vp}(k)}_{n+1} + \Delta\dot{p}^{(k)}_{n+1}\Delta t\boldsymbol{\Lambda}^{\mathrm{vp}(k)}_{n+1}. \tag{3.19}$$

These three inelastic strains and the updated elastic stiffness are used in (3.1) to calculate an updated stress, which is itself used to calculate the updated transformation and yield functions. The iterative scheme then continues until $\varPhi^{t(k+1)}_{n+1}$ and $\varPhi^{\mathrm{vp}(k+1)}_{n+1}$ are smaller than some tolerance.

Because this numerical solution method follows from similar developments for multi-surface plasticity, we must further address a caveat that has been carefully addressed for that discipline (see, for example, Simo and Hughes, 1998, Section 5.2, especially Remark 5.21). Due to potential intersection of the active transformation surface with the viscoplastic constraint function in stress space and further due to the prediction/correction form of the algorithm, predicted violation of a constraint $\Phi^{\mathrm{t}} \leqslant 0$ or $\Phi^{\mathrm{vp}} \leqslant 0$ does *not* necessarily imply that the associated internal variables will meaningfully evolve over the current load increment. After applying the above algorithm until convergence, the signs of $\Delta\xi_{n+1}$ and $\dot{p}_{n+1}$ should be checked for meaningfulness (i.e., $\dot{p}_{n+1} > 0$ and $\Delta\xi_{n+1} > 0$ for forward transformation or $\Delta\xi_{n+1} < 0$ for reverse transformation). In the case that one of these is predicted to evolve in a physically meaningless direction for a given loading increment, the algorithm should be reapplied using (3.12) or (3.14), as applicable, with the incorrect increment nulled.

3.2. Continuum tangent moduli

In addition to requiring the updated thermomechanical state of the material (updated stress and internal variables), the global FEA solver also requires the tangent modulus that defines the current rate of change of stress with a change in total strain, given by

$$\mathrm{d}\boldsymbol{\sigma}_{n+1} = \mathscr{L}\,\mathrm{d}\boldsymbol{\varepsilon}_{n+1}, \tag{3.20}$$

where $\mathscr{L}$ is the tangent stiffness tensor. Coupled thermal and mechanical analysis (i.e., thermomechanical analysis including heat transfer) also requires the thermal tangent modulus, though this is not addressed in this work. It is explained in the literatures (Simo and Hughes, 1998; Qidwai and Lagoudas, 2000) that the convex cutting plane form of the RMA utilizes the *continuum tangent modulus*. The derivation of the continuum tangent modulus for simultaneous processes proceeds as follows.

To begin, the constitutive relation (2.5) is rewritten in differential form and the evolution equation (2.9) are substituted, noting that the increment in time is a user-specified solution parameter and is not subject to algorithmic determination. Rewriting in terms of stress, this gives (cf. (3.5))

$$\mathrm{d}\boldsymbol{\sigma} = \mathscr{C} : \left[\mathrm{d}\boldsymbol{\varepsilon} - \boldsymbol{\alpha}\,\mathrm{d}T \mp \mathrm{d}\xi\left(\partial_{\boldsymbol{\sigma}}\Phi^{\mathrm{t}} + D\left(\boldsymbol{\Lambda}^{\mathrm{t}} + \boldsymbol{\Lambda}^{\mathrm{tp}}\right)\right) - \mathrm{d}\dot{p}\,\boldsymbol{\Lambda}^{\mathrm{vp}}\Delta t\right]. \tag{3.21}$$

Both the transformation function (2.16) and the viscoplastic constraint equation (3.6) must be satisfied for all acceptable solutions, and taking the differential of these relations at a specified constant temperature ($\mathrm{d}T = 0$) results in two relations (analogous to the classical "consistency conditions")

$$\begin{aligned} \mathrm{d}\Phi^{\mathrm{t}} &= \partial_{\boldsymbol{\sigma}}\Phi^{\mathrm{t}} : \mathrm{d}\boldsymbol{\sigma} + \partial_{\xi}\Phi^{\mathrm{t}}\,\mathrm{d}\xi = 0, \\ \mathrm{d}\Phi^{\mathrm{vp}} &= \partial_{\boldsymbol{\sigma}}\Phi^{\mathrm{vp}} : \mathrm{d}\boldsymbol{\sigma} + \partial_{p}\Phi^{\mathrm{vp}}\,\mathrm{d}p + \partial_{\dot{p}}\Phi^{\mathrm{vp}}\,\mathrm{d}\dot{p} = 0, \end{aligned} \tag{3.22}$$

where we note that $\mathrm{d}p = \mathrm{d}\dot{p}\,\Delta t$ for a specified constant time increment Δt. Expressions for the differential of the rate of effective viscoplastic strain $\mathrm{d}\dot{p}$ and the martensitic volume fraction $\mathrm{d}\xi$ are obtained by substituting $\mathrm{d}\boldsymbol{\sigma}$ from (3.21) into (3.22). Noting the form of Φ^{vp} and the definitions of A_1^{t} and A_2^{t} as given in (3.13) and of A_1^{vp} and A_2^{vp} as given in (3.15), this gives

$$\mathrm{d}\xi = \frac{-\partial_{\boldsymbol{\sigma}}\Phi^{\mathrm{t}} : \mathscr{C}\,\mathrm{d}\boldsymbol{\varepsilon} + A_1^{\mathrm{t}}\,\mathrm{d}\dot{p}}{A_2^{\mathrm{t}}}, \tag{3.23}$$

$$\mathrm{d}\dot{p} = \frac{-\partial_{\boldsymbol{\sigma}}\lambda^{\mathrm{vp}} : \mathscr{C}\,\mathrm{d}\boldsymbol{\varepsilon} + A_1^{\mathrm{vp}}\,\mathrm{d}\xi}{A_2^{\mathrm{vp}}}. \tag{3.24}$$

Solving the two equations (3.23) and (3.24) for the two unknowns $\mathrm{d}\xi$ and $\mathrm{d}\dot{p}$, we find for transformation

$$\mathrm{d}\xi = \frac{-A_2^{\mathrm{vp}}\partial_{\boldsymbol{\sigma}}\Phi^{\mathrm{t}} : \mathscr{C}\,\mathrm{d}\boldsymbol{\varepsilon} - A_1^{\mathrm{t}}\partial_{\boldsymbol{\sigma}}\lambda^{\mathrm{vp}} : \mathscr{C}\,\mathrm{d}\boldsymbol{\varepsilon}}{A_2^{\mathrm{t}}A_2^{\mathrm{vp}} - A_1^{\mathrm{t}}A_1^{\mathrm{vp}}}, \tag{3.25}$$

while for viscoplastic processes, the differential is given as

$$\mathrm{d}\dot{p} = \frac{-A_2^{\mathrm{t}}\partial_{\boldsymbol{\sigma}}\lambda^{\mathrm{vp}} : \mathscr{C}\,\mathrm{d}\boldsymbol{\varepsilon} - A_1^{\mathrm{vp}}\partial_{\boldsymbol{\sigma}}\Phi^{\mathrm{t}} : \mathscr{C}\,\mathrm{d}\boldsymbol{\varepsilon}}{A_2^{\mathrm{t}}A_2^{\mathrm{vp}} - A_1^{\mathrm{t}}A_1^{\mathrm{vp}}}. \tag{3.26}$$

Now (3.25) and (3.26) can be used to eliminate $\mathrm{d}\xi$ and $\mathrm{d}\dot{p}$, respectively, in (3.21), giving

$$\begin{aligned} \mathrm{d}\boldsymbol{\sigma} = \mathscr{C}\,\mathrm{d}\boldsymbol{\varepsilon} &\pm \mathscr{C}\left[\frac{A_2^{\mathrm{vp}}\partial_{\boldsymbol{\sigma}}\Phi^{\mathrm{t}} : \mathscr{C}\,\mathrm{d}\boldsymbol{\varepsilon} + A_1^{\mathrm{t}}\partial_{\boldsymbol{\sigma}}\lambda^{\mathrm{vp}} : \mathscr{C}\,\mathrm{d}\boldsymbol{\varepsilon}}{A_2^{\mathrm{t}}A_2^{\mathrm{vp}} - A_1^{\mathrm{t}}A_1^{\mathrm{vp}}}\left(\partial_{\boldsymbol{\sigma}}\Phi^{\mathrm{t}} + D\left(\boldsymbol{\Lambda}^{\mathrm{t}} + \boldsymbol{\Lambda}^{\mathrm{tp}}\right)\right)\right] \\ &+ \mathscr{C}\left[\frac{A_2^{\mathrm{t}}\partial_{\boldsymbol{\sigma}}\lambda^{\mathrm{vp}} : \mathscr{C}\,\mathrm{d}\boldsymbol{\varepsilon} + A_1^{\mathrm{vp}}\partial_{\boldsymbol{\sigma}}\Phi^{\mathrm{t}} : \mathscr{C}\,\mathrm{d}\boldsymbol{\varepsilon}}{A_2^{\mathrm{t}}A_2^{\mathrm{vp}} - A_1^{\mathrm{t}}A_1^{\mathrm{vp}}}\boldsymbol{\Lambda}^{\mathrm{vp}}\Delta t\right]. \end{aligned} \tag{3.27}$$

By applying the definition and identities related to the tensor product (Gurtin, 1981), this can be rearranged to find the continuum tangent modulus, given by $\mathscr{L}$ per[9]

---

[9] The $\otimes$ operator is defined such that, for any two second-order tensors $\mathbf{V}$ and $\mathbf{W}$ (written V_{ij} and W_{ij} in index notation, respectively), $\mathbf{V} \otimes \mathbf{W} = \mathscr{A}$, where $\mathscr{A}$ is a fourth-order tensor with components $\mathscr{A}_{ijkl} = V_{ij}W_{kl}$.

Table 2
Return mapping algorithm for simultaneous transformation–viscoplasticity.

```
1. Initialize
    a. Rotate all tensors from last increment $n$ by $\mathscr{Q}_{n+1}$
    b. Let $k = 0$, $\mathbf{x}_{n+1}^{(0)} = \mathbf{x}_n$ where $\mathbf{x} = \{\xi, \boldsymbol{\varepsilon}^{\mathrm{t}}, \boldsymbol{\varepsilon}^{\mathrm{tp}}, \dot{p}, p, \boldsymbol{\varepsilon}^{\mathrm{vp}}, \mathscr{C}, \boldsymbol{\alpha}\}$
2. Elastic prediction
    a. $\boldsymbol{\sigma}_{n+1}^{(0)} = \mathscr{C}_{n+1}^{(0)}\left[\boldsymbol{\varepsilon}_{n+1} - \boldsymbol{\alpha}(T_{n+1} - T_0) - \boldsymbol{\varepsilon}_{n+1}^{t(0)} - \boldsymbol{\varepsilon}_{n+1}^{\mathrm{tp}(0)} - \boldsymbol{\varepsilon}_{n+1}^{\mathrm{vp}(0)}\right]$
    b. Find $\Phi_{n+1}^{t(0)}$ and $\lambda_{n+1}^{\mathrm{vp}(0)}$
    c. IF $\Phi_{n+1}^{t(0)} \leqslant 0$ AND $\lambda_{n+1}^{\mathrm{vp}(0)} = 0$ THEN EXIT (response elastic)
3. Transformation correction (no viscoplastic deformation)
    a. IF $\Phi_{n+1}^{t(0)} > 0$ AND $f_{n+1}^{p(0)} = 0$ THEN CONTINUE ELSE GOTO 4
    b. Find $\Delta\xi_{n+1}^{(k)}$ via (3.12) with $\Delta\dot{p}_{n+1}^{(k)} = 0$
    c. Find $\xi_{n+1}^{(k+1)}$ per $(3.4)_1$ and $\boldsymbol{\varepsilon}_{n+1}^{t(k+1)}$ and $\boldsymbol{\varepsilon}_{n+1}^{\mathrm{tp}(k+1)}$ per $(3.19)_{1,2}$
    d. IF $\xi_{n+1}^{(k+1)}$ within bounds per (3.18) THEN CONTINUE ELSE set $\xi_{n+1}^{(k+1)}$ to violated bound and set $\Delta\xi_{n+1}^{(k)} = 0$
    e. $\boldsymbol{\sigma}_{n+1}^{(k+1)} = \mathscr{C}_{n+1}^{(k+1)}\left[\boldsymbol{\varepsilon}_{n+1} - \boldsymbol{\alpha}(T_{n+1} - T_0) - \boldsymbol{\varepsilon}_{n+1}^{t(k+1)} - \boldsymbol{\varepsilon}_{n+1}^{\mathrm{tp}(k+1)} - \boldsymbol{\varepsilon}_{vpn}\right]$
    f. IF $\Phi_{n+1}^{t(k+1)} > \mathrm{TOL}^{\mathrm{t}}$ per (2.16) THEN CONTINUE ELSE EXIT
    g. Increment $k$ and GOTO 3b
4. Viscoplastic correction (no transformation)
    a. IF $\lambda_{n+1}^{\mathrm{vp}(0)} > 0$ AND $\Phi_{n+1}^{t(0)} \leqslant 0$ THEN CONTINUE ELSE GOTO 5
    b.–g.: Analogous to 3 above, where $\Phi^{\mathrm{vp}} < \mathrm{TOL}^{\mathrm{vp}}$ indicates convergence
5. Transformation–viscoplastic correction
    a. IF $\lambda_{n+1}^{\mathrm{vp}(0)} > 0$ AND $\Phi_{n+1}^{t(0)} > 0$ THEN CONTINUE ELSE EXIT
    b. Find $\Delta\xi_{n+1}^{(k)}$ and $\Delta\dot{p}_{n+1}^{(k)}$ via (3.16) and (3.17)
    c. Find $\xi_{n+1}^{(k+1)}$ and $\dot{p}_{n+1}^{(k+1)}$ per (3.4), while $p_{n+1}^{(k+1)} = p_n + \Delta t\dot{p}_{n+1}^{(k+1)}$; find $\boldsymbol{\varepsilon}_{n+1}^{t(k+1)}$, $\boldsymbol{\varepsilon}_{n+1}^{\mathrm{tp}(k+1)}$, and $\boldsymbol{\varepsilon}_{n+1}^{\mathrm{vp}(k+1)}$ per (3.19)
    d. IF $\xi_{n+1}^{(k+1)}$ within bounds per (3.18) THEN CONTINUE ELSE set $\xi_{n+1}^{(k+1)}$ to violated bound and set $\Delta\xi_{n+1}^{(k)} = 0$
    e. $\boldsymbol{\sigma}_{n+1}^{(k+1)} = \mathscr{C}_{n+1}^{(k+1)}\left[\boldsymbol{\varepsilon}_{n+1} - \boldsymbol{\alpha}(T_{n+1} - T_0) - \boldsymbol{\varepsilon}_{n+1}^{t(k+1)} - \boldsymbol{\varepsilon}_{n+1}^{\mathrm{tp}(k+1)} - \boldsymbol{\varepsilon}_{n+1}^{vp(k+1)}\right]$
    f. IF $\Phi_{n+1}^{t(k)} > \mathrm{TOL}^{\mathrm{t}}$ OR $\Phi_{n+1}^{\mathrm{vp}(k)} > \mathrm{TOL}^{\mathrm{vp}}$ THEN GOTO 5h
    g. IF $\Delta\xi_{n+1} = \xi_{n+1}^{(k+1)} - \xi_n$ has wrong sign, set $k = 0$ and GOTO 4b ELSE IF $\Delta p_{n+1} = p_{n+1}^{(k+1)} - p_n \leqslant 0$, set $k = 0$ and GOTO 3b ELSE EXIT
    h. Find $\Phi_{n+1}^{t(k+1)}, \Phi_{n+1}^{\mathrm{vp}(k+1)}$ per (2.16) and (B.6), increment $k$, and GOTO 5b
```

$$d\boldsymbol{\sigma} = \left\{\mathscr{C} + \frac{A_2^{\mathrm{t}}\mathbf{B}_1^{\mathrm{vp}} \otimes \mathbf{B}_2^{\mathrm{vp}} + A_1^{\mathrm{vp}}\mathbf{B}_1^{\mathrm{vp}} \otimes \mathbf{B}_2^{\mathrm{t}} \pm \left[A_2^{\mathrm{vp}}\mathbf{B}_1^{\mathrm{t}} \otimes \mathbf{B}_2^{\mathrm{t}} + A_1^{\mathrm{t}}\mathbf{B}_1^{\mathrm{t}} \otimes \mathbf{B}_2^{\mathrm{vp}}\right]}{A_2^{\mathrm{t}}A_2^{\mathrm{vp}} - A_1^{\mathrm{t}}A_1^{\mathrm{vp}}}\right\} d\boldsymbol{\varepsilon} = \mathscr{L}\, d\boldsymbol{\varepsilon}, \tag{3.28}$$

where the second-order tensors $\mathbf{B}_1^{\mathrm{t}}$, $\mathbf{B}_2^{\mathrm{t}}$, $\mathbf{B}_1^{\mathrm{vp}}$, and $\mathbf{B}_2^{\mathrm{vp}}$ are defined as

$$\begin{aligned} &\mathbf{B}_1^{\mathrm{t}} = \mathscr{C}\left(\partial_{\boldsymbol{\sigma}}\Phi^{\mathrm{t}} + D\left(\boldsymbol{\Lambda}^{\mathrm{t}} + \boldsymbol{\Lambda}^{\mathrm{tp}}\right)\right); \quad \mathbf{B}_2^{\mathrm{t}} = \mathscr{C}\partial_{\boldsymbol{\sigma}}\Phi^{\mathrm{t}}; \\ &\mathbf{B}_1^{\mathrm{vp}} = \mathscr{C}\boldsymbol{\Lambda}^{\mathrm{vp}}\Delta t; \quad \mathbf{B}_2^{\mathrm{vp}} = \mathscr{C}\partial_{\boldsymbol{\sigma}}\lambda^{\mathrm{vp}}. \end{aligned} \tag{3.29}$$

Table 2 provides a summary of the full RMA (convex cutting plane) needed to integrate the constitutive relations for the transformation–viscoplastic yield model in an FEA framework.[10]

4. Three-dimensional computational analysis

To demonstrate the capabilities of this new tool, the implemented model of Section 3 is used to predict the response of three different bodies subjected to varying thermal and mechanical inputs. The Abaqus Unified Finite Element framework (Abaqus, 2007a) was chosen as the global solver for its robustness in considering non-linearities such as contact and large deformations, both of which are considered here. The non-linear material behavior is modeled by implementing the numerical algorithms described above, including the tangent modulus, in an Abaqus-specific form of user material subroutine, known as a "UMAT".

The first analysis considered is associated with experimental results and demonstrates the ability of the model and implementation to capture a known data set and then to predict the evolution of an unknown one. Simplified calibration and full 3-D analysis are both considered. The second 3-D analysis, sharing the material properties from the first, examines the response of a HTSMA spring undergoing relatively large deflections. Finally, we demonstrate the utility of this new model in capturing the shape-setting behavior in conventional SMAs (i.e., near-equiatomic NiTi).

---

[10] For the consideration of large structural rotations, the discussion of Hartl and Lagoudas (2009), Appendix A is applicable. A computation is added as the first step in Table 2, whereby the tensorial internal variables are properly rotated into a current reference frame for each loading step.

4.1. Calibration of the 3-D model

To begin, the results from an experimental study of an HTSMA with a composition of $Ti_{50}Pd_{40}Ni_{10}$ (Kumar and Lagoudas, 2009) are used to calibrate the 3-D model. The results from conventional creep tests and isobaric actuation experiments are both used. For each experiment type, the nominal strain data are derived from the change in length of a cylindrical specimen (6 mm in diameter, 12 mm in length), and the nominal stress is taken from the total applied force normalized by specimen cross-sectional area. During isobaric loading, these specimens were subjected to constant nominal compressive loads (100 MPa and 200 MPa), where the temperature rate during cooling and heating was 2 °C/min. The derived properties are given in Table 3. The thermoelastic properties consist of the following: (i) the *Young's moduli* for austenite and martensite (E^{A} and E^{M}) are taken from the loading and unloading of the two phases in pre-tests, (ii) the *Poisson's ratio* for the two phases (ν^{A} and ν^{M}) are taken from the literature, and (iii) a common *coefficient of thermal expansion* (α) is taken from strain–temperature testing (i.e., the isobaric results). Note that in this particular material, the observed modulus of martensite exceeds that of austenite, which is not common in SMAs (Otsuka and Wayman, 1999). The configuration of the phase diagram (Lagoudas, 2008) is described by the four *transformation temperatures* (M^{s}, M^{f}, A^{s}, and A^{f}) and the forward and reverse *stress influence coefficients* or slopes of the transformation surfaces (C^{M} and C^{A}). The maximum transformation strain function $H^{\mathrm{cur}}(\bar{\sigma})$ is taken from (2.11) and is calibrated by considering the height of the strain–temperature hysteresis (after accounting for elastic effects, creep, and TRIP). The smooth transformation hardening parameters n_1—n_4 were calibrated to match the smooth transition from transformation to thermoelastic response (and vice versa) observed in the strain–temperature hysteresis. The TRIP function $f^{\mathrm{tp}}(\bar{\sigma})$ is calibrated by considering the irrecoverable strain generated during a full transformation cycle after accounting for creep. Finally, the dependencies of the effective viscoplastic strain rate $\dot{p}$ were calibrated from standard creep tests on the pure phases of the material (see Kumar and Lagoudas, 2009). For the thermomechanical paths applied, it was assumed that consideration of an elastic domain was not necessary and that the material hardening was negligible ($f^{\mathrm{vp}}(T,p)=0$). This implies that a suitable form for $K_{\mathrm{a}}(T)$ is that given by (2.20). Further, it was observed that the material exhibited non-negligible creep strains only at temperatures above ≈450 °C. Since the considered temperatures did not exceed 520 °C, the temperature range for creep was considered sufficiently small such that the parameter N_{a} was assumed independent of temperature.

The calibrated model is used to simulate the calibration experiments by analyzing a two-element prismatic bar under compressive loading. The results can be seen in Fig. 1a. Note how the ability to capture smooth transformation hardening increases the accuracy of the simulation. Fig. 1b illustrates the predictive capabilities of the model and implementation by considering additional experiments performed at a higher thermal rate (20 °C/min), where creep is less pronounced. Recall that the model was calibrated using only 2 °C/min data.

4.2. 3-D analysis 1: actuation response of an HTSMA compression specimen

The experiments and subsequent calibration described in Section 4.1 are dependent on the assumption that the averaged structural response of the compressive testing specimen is representative of the constitutive response of the material itself.

Table 3
The 25 material properties for $Ti_{50}Pd_{40}Ni_{10}$ used to calibrate the new SMA transformation–viscoplastic yield model (derived from isobaric compressive experiments, $\dot{T}=2\ {}^{\circ}\mathrm{C/min}$).

Parameter(s)	Value(s) or functional form(s)
Thermoelastic behavior	
$E^{\mathrm{A}},\ E^{\mathrm{M}}$	32 GPa, 57 GPa
$\nu^{\mathrm{A}}=\nu^{\mathrm{M}}$	0.33
α	2.8E−5/°C
Phase diagram	
$M_{\mathrm{s}},\ M_{\mathrm{f}},\ A_{\mathrm{s}},\ A_{\mathrm{f}}$	407 °C, 350 °C, 372 °C, 456 °C
$C^{\mathrm{M}}\big\vert_{\bar{\sigma}=150\,\mathrm{MPa}},\ C^{\mathrm{A}}\big\vert_{\bar{\sigma}=150\,\mathrm{MPa}}$	12.0 MPa/°C, 6.0 MPa/°C
Maximum transformation strain and smooth hardening	
$H^{\mathrm{cur}}(\bar{\sigma})$	$=0.0042+0.0478\left(1-\exp\left(240\bar{\sigma}/E^{\mathrm{A}}\right)\right)$
$n_1,\ n_2,\ n_3,\ n_4$	0.30, 0.10, 0.20, 0.25
Transformation-induced plastic strain	
$f^{\mathrm{tp}}(\bar{\sigma})$	$=(9.00E-5)-\left(0.640/E^{\mathrm{A}}\right)\bar{\sigma}+\left(410/E^{\mathrm{A}^2}\right)\bar{\sigma}^2$
Viscoplastic modeling constants	
$K_{\mathrm{a}}(T)$	Taken from the form of (2.20)
A	$0.1368\ \mathrm{MPa}^{-N_{\mathrm{a}}}\ \mathrm{s}^{-1}$
Q	$197.7\ \mathrm{kJ\ mol}^{-1}$
R	$0.00831\ \mathrm{kJ\ K}^{-1}\ \mathrm{mol}^{-1}$
N_{a}	4

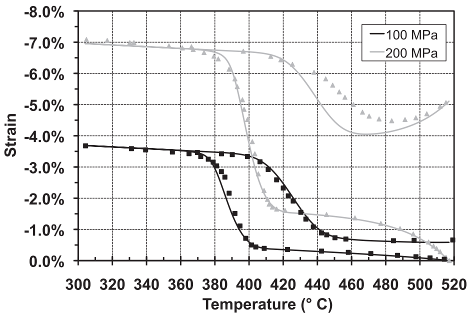

(a) Experimental results and numerical *simulation* (2 °C/min)

(b) Experimental results and numerical *prediction* (20 °C/min)

Fig. 1. Compressive strain/temperature response of a $Ti_{50}Pd_{40}Ni_{10}$ HTSMA under constant applied stresses given two applied temperature rates.

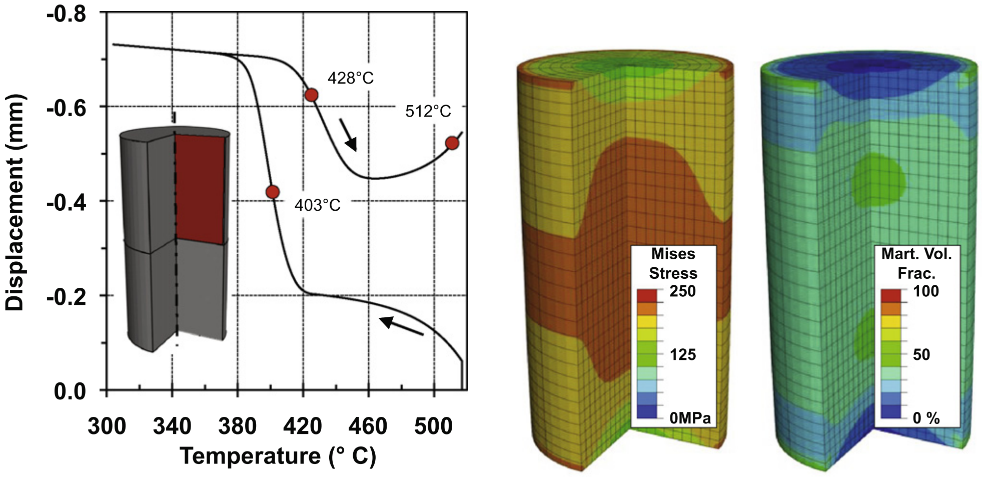

(a) Thermomechanical loading cycle and cylinder reference configuration (axisymmetric computational domain highlighted)

(b) Mises stress and martensitic volume fraction distributions at 403 °C during cooling

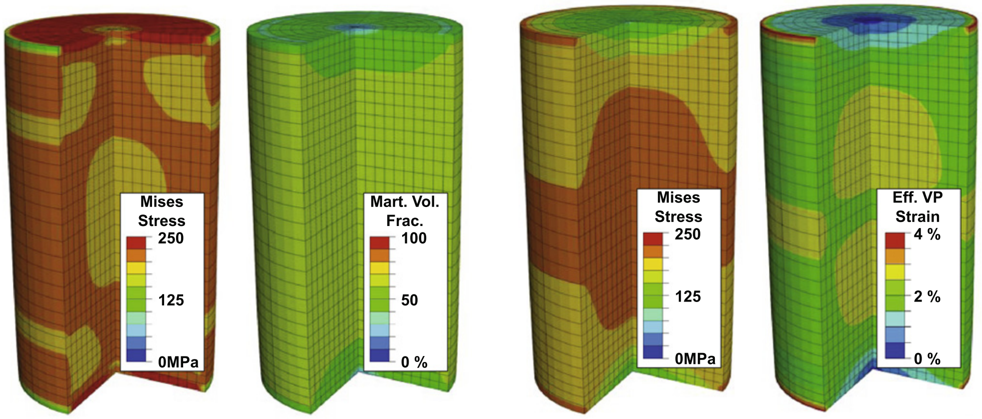

(c) Mises stress and martensitic volume fraction distributions at 428 °C during heating

(d) Mises stress and effective viscoplastic strain distributions at 512 °C during heating

Fig. 2. Numerical results for isobaric thermal cycling of a compression specimen illustrating non-homogeneous distribution of solution fields.

Such an assumption is especially suitable for tensile testing because common wire or "dogbone" specimens provide a geometrically homogeneous gauge section sufficiently distanced from stress concentrations at the grips. Compression testing, however, does not allow for long gauge sections as high aspect ratio specimens buckle more easily than those with a low aspect ratio. An example minimum recommended aspect ratio is 2:1 (length to diameter) (ASTM, 2000), as was used in the currently considered experimental effort (Kumar and Lagoudas, 2009). In this example, the same compressive testing specimen is analyzed given the same thermomechanical loading path applied during experimentation to investigate the effects that 3-D loading conditions have on the internal and averaged responses. This allows one to assess the accuracy of the properties derived from the low aspect ratio specimen in describing *constitutive* response.

The boundary value problem consists of loading a solid cylinder in compression where the cylinder dimensions match those of the experimental specimen. The specimen is modeled assuming both axisymmetry and a symmetric bisection of the specimen length. The compression grip is modeled as a rigid planar surface. Abaqus contact algorithms were utilized to account for the grip-specimen interface (Abaqus, 2007a), and a coefficient of friction of 0.2, determined from experiments, is assumed. A 200 MPa nominal constant stress is applied by specifying a 5655 N total downward force on the reference point of the rigid grip surface. With this force held constant, a spatially homogenous temperature evolution was then applied with the same average rate as was used during the calibration experiments (2 °C/min).

The results of this analysis are shown in Figs. 2 and 3. The predicted evolution in grip displacement is illustrated in Fig. 2a. The distribution of equivalent (or Mises) stress $\bar{\sigma}$ and martensitic volume fraction ξ during forward and reverse transformation are shown in Fig. 2b and c, while the stress and effective viscoplastic strain (p) distributions are shown in Fig. 2d (reverse transformation completed). Clearly the solution fields are not spatially homogeneous, indicating that the average response of the specimen may not be representative of the constitutive response of the material. In Fig. 3, the predicted deformation response of the compressive specimen (grey line) is compared to the original experimental results. A small error is observed in the amount of recoverable transformation strain, and this differs from Fig. 1 (where an almost perfect match is observed). This deviation from the calibration results of Fig. 1 is yet another illustration of how the 3-D numerical implementation of the model captures spatial inhomogeneities such as stress concentrations while the 1-D idealizations applied during calibration do not. Thus, the FEA analysis tool is useful not only in the prediction of structural behavior in proposed applications, but it may also have a role in the proper interpretation of some experimental results where assumptions of homogeneous response do not apply.

4.3. 3-D analysis 2: actuation response of an HTSMA spring

Here we expand on the previous analysis by considering the same HTSMA material ($Ti_{50}Pd_{40}Ni_{10}$) utilized in a different, more structurally complex application: a helical spring providing thermally induced actuation. It is described in the work on HTSMA springs by Stebner et al. (2009) that methods such as drawing or precision grinding can be used to reduce HTSMA rods to wire form. Springs, like beams, provide a structural method of maximizing the deflections attainable from even moderate transformation strains. However, in the case of HTSMAs, the effects of rate-dependent irrecoverable strains are also magnified and must be considered. The analysis of conventional SMA springs has been performed by other researchers, and large deformation formulations have been employed (Toi et al., 2004; Auricchio and Petrini, 2004), though rate-dependent irrecoverable strains have not been considered to date.

Motivated by the work by Stebner et al. (2009), the spring modeled here has a coil diameter of 12.7 mm, a wire diameter of 0.5 mm, and a spring pitch of 2.8 mm. One full coil (or "turn") is modeled in a fully three-dimensional space using second-order hexahedral elements with reduced integration (Abaqus designation `C3D20R`). The single coil is discretized such that its length is divided into 150 uniform segments while 32 elements make up the cross-section, resulting in 4800 total elements. The boundary conditions consist of fixing the nodes at one end of the spring wire while applying a downward biasing force (parallel to the axis of the spring) to the other end of the spring wire. The reference geometry, the mesh through the cross-

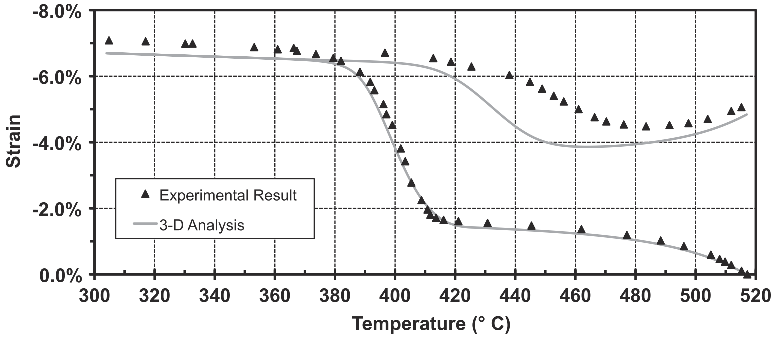

Fig. 3. Comparison of experimental compression testing results for $Ti_{50}Pd_{40}Ni_{10}$ to results of 3-D analysis applied to the same specimen given the original parameters of Table 3 (grey line).

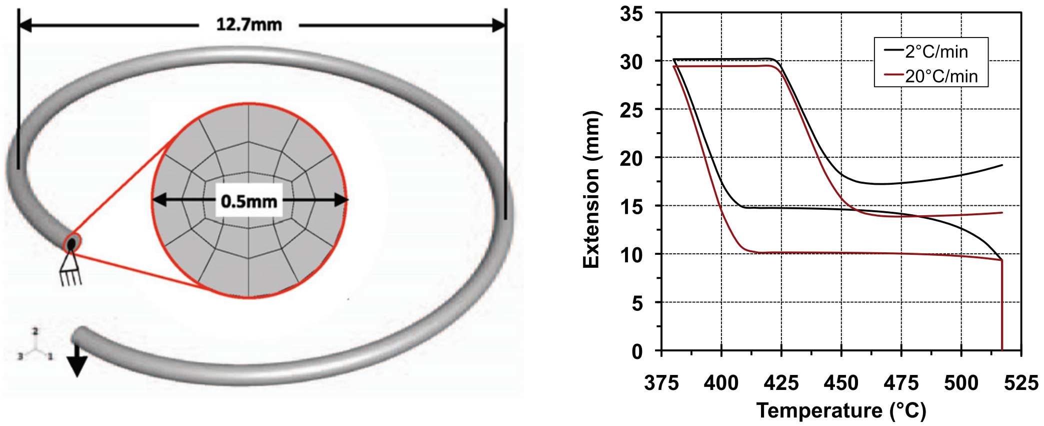

(a) Initial geometric configuration (including cross-sectional mesh) and applied boundary conditions

(b) Spring extension over thermal cycle (2 °C/min and 20 °C/min heating/cooling rates)

Fig. 4. Reference geometry, boundary conditions, and thermally induced actuation results for the analysis of an HTSMA extensional spring under 0.25 N biasing load.

section, and the applied boundary conditions are shown in Fig. 4a. The full thermomechanical loading path proceeds as follows:

1. Apply 0.25 N biasing load at $T = 517$ °C (material is austenitic, length of step is 1 s).
2. Maintaining the biasing load, cool spring uniformly to $T = 380$ °C at constant rate.
3. Maintaining the biasing load, heat spring uniformly to $T = 517$ °C at constant rate.

In agreement with observed SMA spring behavior, this analysis predicts substantial deformation of the spring during actuation from an initially coiled shape towards a straight wire configuration. Though the local strains never exceed 2.6% at any point, non-linear geometric effects are clearly important, especially the local rotations undergone by each material point. These rotations are accounted for by ensuring that the algorithm of Section 3 is implemented in an "incrementally objective" manner (Hughes and Winget, 1980) and by activating the non-linear geometry flag in the global solver (option `NLGEOM` = `YES` in Abaqus). This is described in more detail in the work by Hartl and Lagoudas (2009) (Appendix A). The large rotations also result in non-proportional loading with moderate changes in local stress directions during transformations. However, it was observed that local stress magnitudes decreased substantially during cooling, and this is expected to preclude any reorientation of martensite, preserving the applicability of (2.9).

The analysis results for the extension of the single-coil HTSMA spring given this loading path are shown in Fig. 4b for temperature rates of 2 °C/min and 20 °C/min (cf. Section 4.2). As with the analysis of the compression specimen, the 2 °C/min rate is sufficiently slow to allow the spring to viscoplastically creep during cooling at $T > 450$ °C. Additional creep is observed during heating back to 517 °C. The 20 °C/min rate results in less creep and thus less overall loss in recoverable actuation.

Another more interesting result highlights the coupling that exists between the transformation-induced strains and the viscoplastic strain. By examining the "gap" in the hysteresis at $T \approx 470$ °C, it is clear that the slower thermal rate, which leads to more creep overall, results in *less* irrecoverable strain due to TRIP. In other words, less transformation-induced plastic strain has been generated due to an increase in generated viscoplastic strain. This is because the viscoplastic strain serves to relax the stresses where they are at their highest, homogenizing the stress state through the cross-section. Because the magnitude of TRIP strain is related to the square of the local stress magnitude (see the form of f^{tp} in Table 3), viscoplastic relaxation of the stress near the wires surface results in decreased TRIP strain generation.

Detailed analysis results for the case of 2 °C/min cooling and heating are provided in Fig. 5. Here the deformation of the single-coil spring is shown at various points along the loading path (highlighted in Fig. 5a). The slow cooling at high temperatures ($T > 450$ °C) leads to the generation of viscoplastic strains throughout the spring, especially at its mid-length where torsional loads are the highest. Examining the cross-section at this point shows that the highest viscoplastic strains are generated on the surface of the wire as expected, where stresses are maximized. The same trend is observed in the distribution of martensitic volume fraction as the spring begins to transform (Fig. 5b). Substantial extension is observed during spring actuation although full forward transformation is not completed. As the spring is heated and reverse transformation begins, we see that the viscoplastic strains have not evolved appreciably but that the martensitic volume fraction at the wire surface has reached ≈50% (Fig. 5c). Finally, as the spring is heated back toward its initial temperature, all martensite is transformed once again into austenite and a substantial portion of the deformation is recovered. However, additional viscoplastic strains

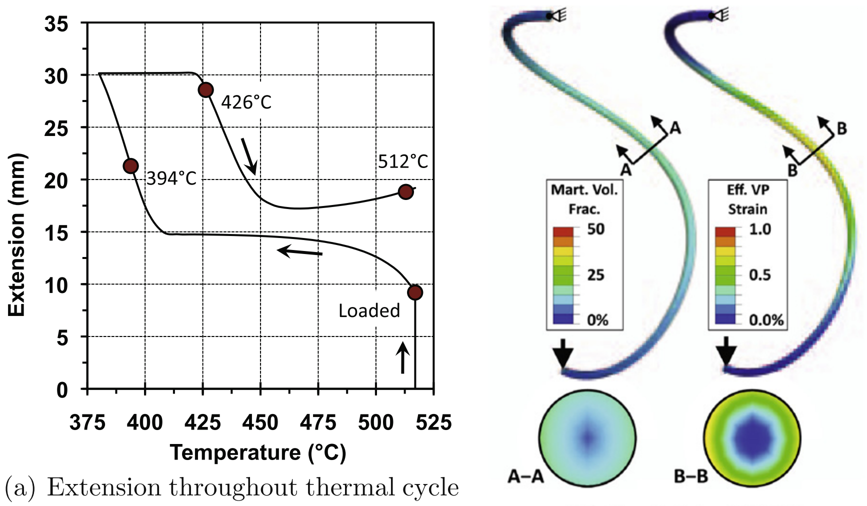

(a) Extension throughout thermal cycle applied to spring

(b) Cooled to 394 °C

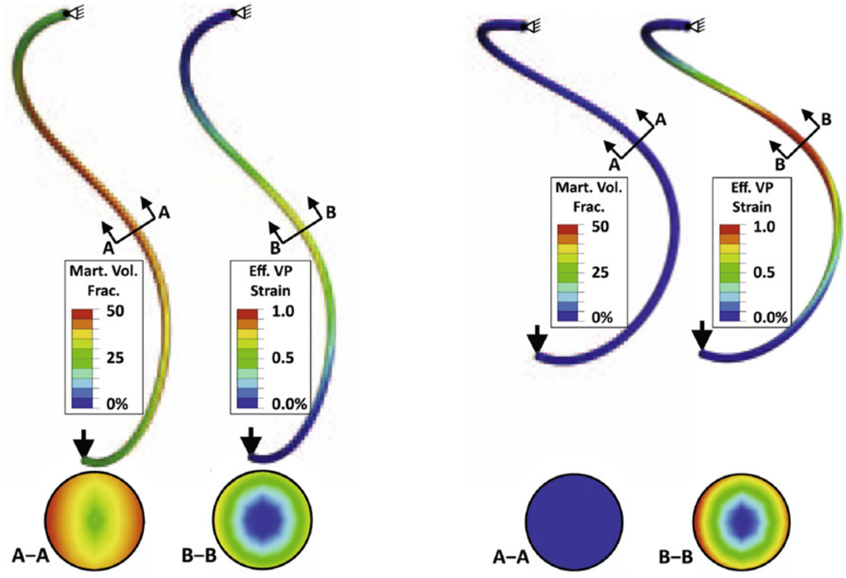

(c) Heated to 426 °C

(d) Heated to 512 °C

Fig. 5. Evolution of martensitic volume fraction (ξ) and effective viscoplastic strain (p) for HTSMA spring heated and cooled at 2 °C/min (contour/deformation plots all of equal scale).

are generated (exceeding 1% in some local material regions); The combination of viscoplastic and TRIP strains results in irrecoverable spring deformation (Fig. 5d).

4.4. 3-D analysis 3: shape-setting of a pseudoelastic SMA stent

For the last of the 3-D analyses considered herein, we shift our focus away from HTSMAs and consider instead the behavior of a near-equiatomic NiTi pseudoelastic medical stent during device processing. These devices represent the most prolific use of SMAs in the medical industry and are among one of the most well-known SMA applications (Mantovani, 2000; Machado and Savi, 2003). Some stent configurations are formed by first laser-cutting the complex structural forms from solid tubes of relatively small diameter (Morgan, 2004). An expansion step increases the stent diameter, which is then constrained in this expanded configuration. Exposure to high temperatures for some span of time relaxes the stresses generated during expansion, and, upon cooling and removal of the diameter constraints, a new unconstrained diameter is observed. This process of altering the force-free reference shape of an SMA structure by constraint and exposure to elevated temperatures is known as *shape-setting* (Morgan, 2004).

For the current analysis, nominal NiTi properties have been used to describe the conventional (i.e., fully recoverable) transformation behavior of the material (see the text by Lagoudas (2008, Table 2.4)). The effects of TRIP, which can be minor in high quality medical-grade NiTi, are not considered. The viscoplastic model parameters were taken from the work of Kobus et al. (2002) as interpreted by Oppenheimer et al. (2007) (Table 2 and Fig. 2). Of the viscoplastic studies performed on NiTi, the work of Kobus and co-workers considers temperatures and stress levels most applicable to common shape-setting conditions (i.e., $T \approx 500\,^{\circ}\mathrm{C}$). Specifically, if we consider the forms of (2.18) and (2.20), the viscoplastic material properties are described by

$$A = 1.0E11\ \mathrm{MPa}^{-N_a}\ \mathrm{s}^{-1}; \quad Q = 421.0\ \mathrm{kJ\ mol}^{-1}; \quad R = 0.00831\ \mathrm{kJ\ K}^{-1}\ \mathrm{mol}^{-1}; \quad N_a = 5.$$

The full 3-D FEA model for the medical stent was obtained from Abaqus, and is available to the public as a benchmarking problem. Here we consider the periodic axisymmetry of the structure and model two "legs" only; the model is meshed with 672 quadratic hexahedral elements with reduced integration (Abaqus designation `C3D20R`). Four elements are used through the bending thickness. The initial reference mesh is shown in Fig. 6a, where the computational domain (two legs) is highlighted. The large rotations experienced by the stent legs are accounted for by considering the same non-linear geometric effects as the previous analysis.

The thermomechanical loading path considered here is based on the common NiTi shape-setting process previously described. After shape setting, the device is taken through an additional crimp-release cycle to demonstrate the usefulness of the numerical tool in capturing both the shape setting and stress-induced transformation in a single multi-step analysis. The overall thermomechanical loading path is shown in Fig. 6b, where the temperature and outer diameter (OD) are plotted vs. time. The imposed thermal and boundary conditions applied during this one continuous analysis are as follows:

1. Shape-setting
    (a) Increase stent outer diameter from $D = 1.47$ mm to $D = 6.04$ mm at $T = 22\,^{\circ}\mathrm{C}$ (length of step: 1 min).
    (b) With diameter constrained, heat stent uniformly to $T = 500\,^{\circ}\mathrm{C}$ (length of step: 5 min).
    (c) Maintain $T = 500\,^{\circ}\mathrm{C}$ (length of step: 5 min).
    (d) Cool uniformly to $T = 37\,^{\circ}\mathrm{C}$ (length of step: 5 min).
    (e) Release diameter constraints at $T = 37\,^{\circ}\mathrm{C}$ (length of step: 1 min).
2. Crimping and free deployment
    (a) Decrease stent outer diameter to $D = 1.47$ mm at $T = 37\,^{\circ}\mathrm{C}$ (length of step: 30 s).
    (b) Release diameter constraints at $T = 37\,^{\circ}\mathrm{C}$ (length of step: 30 s).

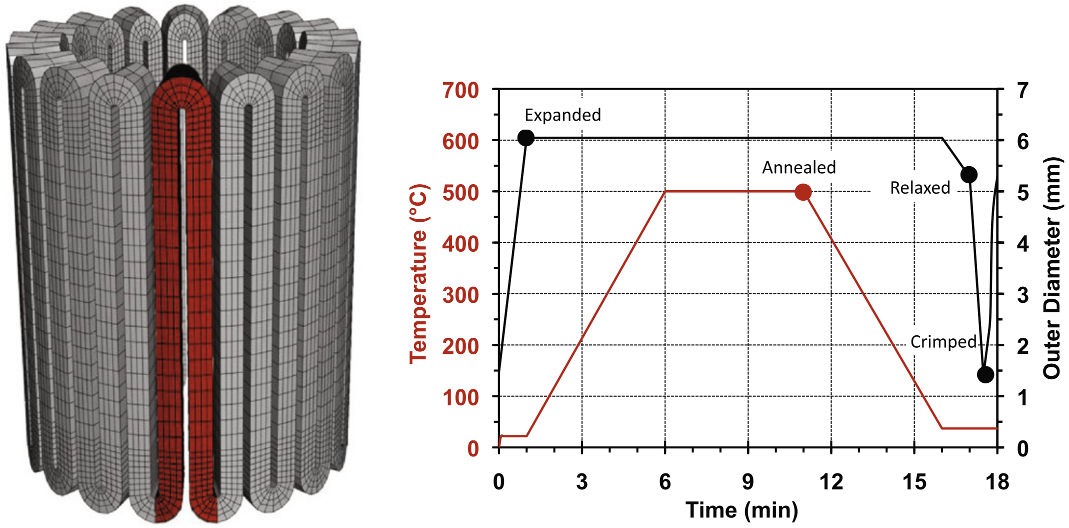

(a) Initial geometric configuration (computational domain highlighted)

(b) Thermomechanical loading path applied

Fig. 6. Reference geometry and thermomechanical loading path for the analysis of shape setting in an NiTi medical stent.

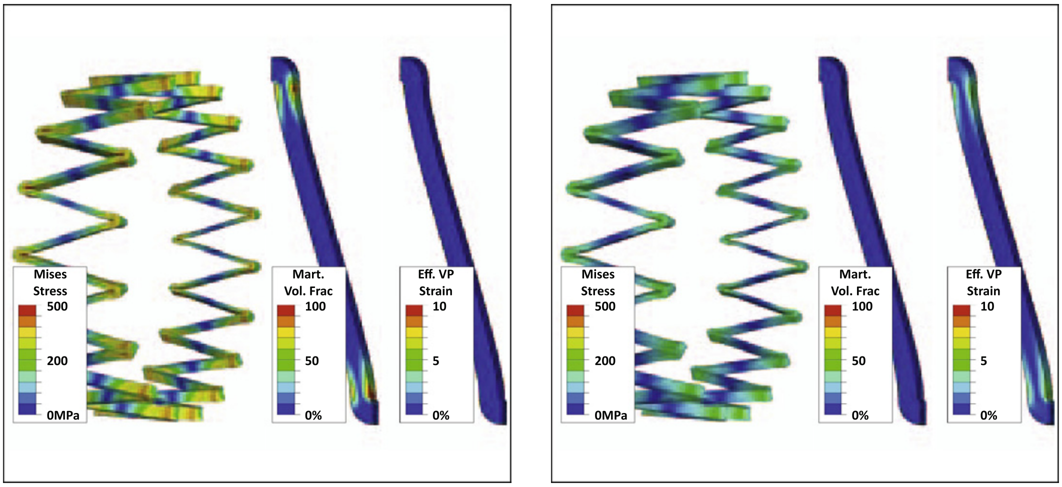

(a) Expanded (b) Annealed

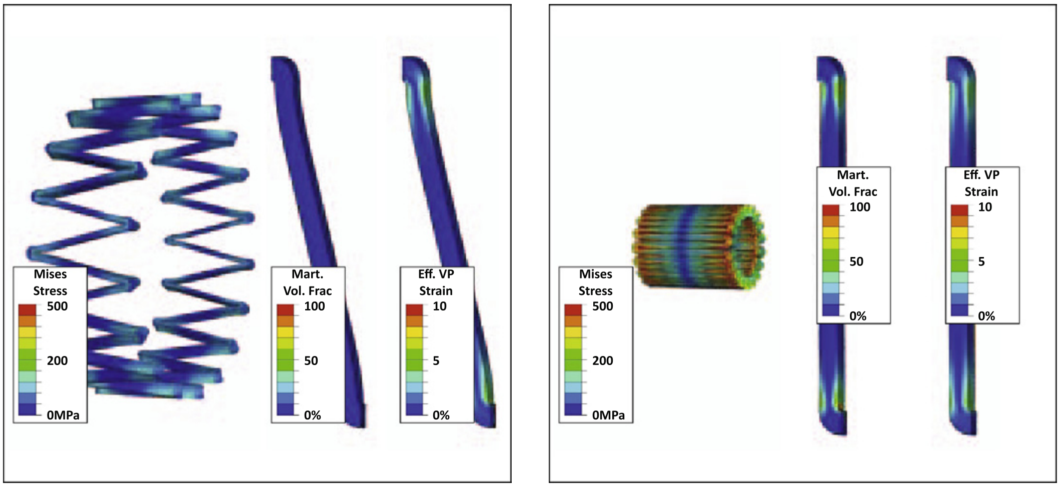

(c) Relaxed (d) Crimped

Fig. 7. Analysis results for the shape-setting and subsequent crimping of an NiTi SMA stent. Contours indicate Mises equivalent stress ($\bar{\sigma}$), martensitic volume fraction (ξ), and effective viscoplastic strain (p) distributions.

The results of the NiTi stent shape-setting analysis are shown in Fig. 7 for four different solution states in the loading path. These states are marked in Fig. 6b. For each state, the deformations of single leg and of the annular array of stent legs are illustrated in addition to the stress, martensitic volume fraction, and effective viscoplastic strain contours. These results are useful in illustrating the qualitative evolution in the state of the SMA stent during shape-setting.

The initial expansion from the reference configuration causes local stresses sufficient to initiate and, in some regions, complete the transformation into martensite (Fig. 7a). Subsequent heating then transforms these regions back into austenite. The process of heating up to and holding at 500 °C over the span of 10 min provides enough thermal energy and elapsed time to allow the generation of viscoplastic strains in the regions of high stresses. This relaxes stresses throughout the stent (Fig. 7b). After cooling, the diameter constraint is removed, reducing the stresses even further. Little additional viscoplastic strain generation occurs during cooling, and the elastic unloading causes a small decrease in the diameter (Fig. 7c). Finally, crimping the stent back toward its reference configuration results in internal effects analogous to the original expansion step: local regions reach high-stress levels, inducing (but not quite completing) the stress-induced martensitic transformation (Fig. 7d).

5. Summary and conclusions

To account for the effects of viscoplastic deformation on the actuation characteristics of 3-D SMA and HTSMA structural elements, a new phenomenological constitutive model has been both derived and implemented for the first time. The new model not only captures rate-dependent viscoplastic yielding in the pure SMA phases (i.e., austenite or martensite); it also considers simultaneous transformation–viscoplastic behavior. This ability is important to those in the smart structures engineering community considering HTSMA materials, where the transformation and creep phenomena are often observed concurrently. The interpretation of HTSMA characterization experiments and especially the analysis of SMA and HTSMA components subjected to high temperatures can each be improved by the use of the modeling methods described above.

The numerical implementation of the new model was described in detail, and it was shown that the same methods that have been used to integrate coupled SMA transformation–plastic yield constitutive equations can also be used when transformation is coupled with rate-dependent viscoplasticity. In particular, the convex cutting plane form of the return mapping algorithm was chosen. It was shown that the implemented model could be accurately calibrated and experimental results from an HTSMA study were predicted.

The new modeling tool was used to perform three 3-D analyses. The first considered a 3-D HTSMA cylindrical compressive specimen and showed that the internal state of such a low aspect ratio specimen is not homogenous along the length or throughout the cross-section. The second considered an HTSMA spring, where simultaneous creep and forward transformation combine to cause substantial deformation (extension) of the spring, only some of which is recovered during transformation back into austenite. Finally, to highlight the uses of the new model with regards to conventional SMAs, the shape setting of an NiTi stent was considered. It was shown that, using creep data for NiTi found in the literature, the salient effects of conventional shape-setting processes can be predicted. Future work will extend the modeling effort to even more complex 3-D domains, including new actuator components. The constitutive model itself may also be extended to consider the effects of time and temperature on the material properties themselves (resulting from the effects of aging and annealing on grain size, precipitate growth, etc.).

Acknowledgments

The authors foremost acknowledge NASA-Glenn, both for their technical input as well as their financial support via project NNX07AB56A. D. Hartl further acknowledges the financial support of the NSF-IGERT fellowship that funded his research. D. Lagoudas acknowledges the TiiMS institute funded by NASA Cooperative Agreement No. NCC-1-02038. The continuing support of The Boeing Company in motivating new application ideas is greatly appreciated.

Appendix A. Calibration of transformation model parameters

Several model parameters described in this work are derived by examining the configuration of the SMA phase diagram, often calibrated using uniaxial testing results (see, for example, Chapter 2 in the work by Lagoudas (2008)). Here we consider that the phase diagram is itself described by six parameters: four *zero-stress* transformation temperatures (M_s, M_f, A_s, and A_f) and two transformation surface slopes, one for forward transformation (C^M) and another for reverse transformation (C^A). These slopes are measured at some common uniaxial reference stress level σ^*, and, in general may differ.

The smooth transformation hardening parameters a_1, a_2, and a_3 and the energetic parameter $\rho\tilde{u}_0$ are calibrated as follows:

$$\begin{aligned}
&a_1 = \rho\tilde{s}_0(M_f - M_s), \quad a_2 = \rho\tilde{s}_0(A_s - A_f),\\
&a_3 = -\frac{a_1}{4}\left(1 + \frac{1}{n_1+1} - \frac{1}{n_2+1}\right) + \frac{a_2}{4}\left(1 + \frac{1}{n_3+1} - \frac{1}{n_4+1}\right),\\
&\rho\tilde{u}_0 = \frac{\rho\tilde{s}_0}{2}(M_s + A_f).
\end{aligned}$$

To account for two different transformation slopes on the phase diagram (i.e., $C^M \neq C^A$), it can be shown that thermodynamic consistency requires the following form for $Y^t(\boldsymbol{\sigma})$:

$$Y^t = Y^t_0 + D\boldsymbol{\sigma} : \left(\boldsymbol{\Lambda}^t + \boldsymbol{\Lambda}^{tp}\right),$$

where, for uniaxial tensile testing ($\sigma = [\boldsymbol{\sigma}]_{11} \geqslant 0$)

$$Y^t_0 = \frac{\rho\tilde{s}_0}{2}(M_s - A_f) - a_3,$$

$$D = \left.\frac{\left(C^M - C^A\right)\left(H^{cur} + \sigma\partial_\sigma H^{cur} + \sigma\widetilde{\mathscr{S}}\right) + \left(C^M + C^A\right)(f^{tp} + \sigma\partial_\sigma f^{tp})}{\left(C^M + C^A\right)(H^{cur} + \sigma\partial_\sigma H^{cur}) + \left(C^M - C^A\right)(f^{tp} + \sigma\partial_\sigma f^{tp})}\right|_{\sigma=\sigma^*}.$$

The final required transformation model parameter $\rho\tilde{s}_0$ is likewise calculated as follows:

$$\rho\tilde{s}_0 = -2\left(C^{\mathrm{M}}C^{\mathrm{A}}\right)\frac{(H^{\mathrm{cur}} + \sigma\partial_\sigma H^{\mathrm{cur}} + \sigma\widetilde{\mathscr{S}})(H^{\mathrm{cur}} + \sigma\partial_\sigma H^{\mathrm{cur}}) - (f^{\mathrm{tp}} + \sigma\partial_\sigma f^{\mathrm{tp}})^2}{\left(C^{\mathrm{M}} + C^{\mathrm{A}}\right)(H^{\mathrm{cur}} + \sigma\partial_\sigma H^{\mathrm{cur}}) + \left(C^{\mathrm{M}} - C^{\mathrm{A}}\right)(f^{\mathrm{tp}} + \sigma\partial_\sigma f^{\mathrm{tp}})}\Bigg|_{\sigma=\sigma^*}.$$

The calibration is simplified substantially if identical transformation slopes ($C^{\mathrm{M}} = C^{\mathrm{A}}$), a constant $H^{\mathrm{cur}}(\sigma) = H$, and no TRIP evolution are assumed (as in most common SMA constitutive models).

Appendix B. Integration of the viscoplastic evolution equation

A fundamental challenge in the numerical implementation of rate-dependent plastic (or viscoplastic) constitutive models is the accurate integration of the evolution equation for the viscoplastic strain, which is non-homogeneous in time. Discretizing $(2.9)_3$ in time, we can use the general trapezoidal rule (Ortiz and Popov, 1985) to solve for the inelastic transformation strain in the current loading step under consideration (i.e., at time t_{n+1}), and this is written as[11]

$$\boldsymbol{\varepsilon}^{\mathrm{vp}}_{n+1} = \boldsymbol{\varepsilon}_n + \Delta t\left[(1-\gamma)\dot{p}_n\boldsymbol{\Lambda}^{\mathrm{vp}}_n + \gamma\dot{p}_{n+1}\boldsymbol{\Lambda}^{\mathrm{vp}}_{n+1}\right], \tag{B.1}$$

where γ is an algorithmic parameter that ranges from 0 to 1. Of course, infinitely many options exist for the value of γ, which is often chosen and then held constant during analysis. Values of $\gamma = 1, \frac{1}{2}, 0$ have been discussed in the literature (Ortiz and Popov, 1985). In the present work, we consider $\gamma = 0$ (known as *forward Euler integration*), and $\gamma = 1$ (known as *backward Euler integration*).

B.1. Option 1: forward Euler integration

A straightforward option is to assume that $\gamma = 0$ and thus that the rate of the viscoplastic strain in the current time step can be approximated explicitly using the solution from the last. To implement this, we use $(2.10)_3$ and (2.18) evaluated at the previous time step, such that

$$\dot{\boldsymbol{\varepsilon}}^{\mathrm{vp}} = \left(\dot{\boldsymbol{\varepsilon}}^{\mathrm{vp}}\right)_n = \lambda^{\mathrm{vp}}(\boldsymbol{\sigma}_n, T_{n+1}, p_n)\boldsymbol{\Lambda}^{\mathrm{vp}}(\boldsymbol{\sigma}_n). \tag{B.2}$$

Clearly this allows for simplified coding and rapid calculation, and some commercial FEA packages employ this option for materials where the rate of creep is slow compared to the time scale of the analysis and time steps are sufficiently small (Abaqus, 2007b). For higher creep rates, however, very small time steps are required to achieve accuracy. Further, for values of $\gamma < \frac{1}{2}$ (as is considered here with $\gamma = 0$), the integration algorithm can become unstable and thus may not converge to the correct solution (Ortiz and Popov, 1985). The Backward Euler methods is chosen as the more robust option.

B.2. Option 2: backward Euler integration (direct iteration)

In general, backward Euler integration is performed by using $\gamma = 1$ in the discretized evolution equation (B.1). This makes it implicit in time and gives

$$\boldsymbol{\varepsilon}^{\mathrm{vp}}_{n+1} = \boldsymbol{\varepsilon}^{\mathrm{vp}}_n + \Delta t\dot{p}_{n+1}\boldsymbol{\Lambda}^{\mathrm{vp}}(\boldsymbol{\sigma}_{n+1}). \tag{B.3}$$

This relation must be solved implicitly, and one scheme for doing so is to use *direct iteration* or *fixed-point iteration* (for a general treatment, see the discussions of Reddy (2004)). Specifically, (2.18) is used to define $\dot{p}$ and then (B.3) is solved iteratively, giving

$$\boldsymbol{\varepsilon}^{\mathrm{vp}(k+1)}_{n+1} = \boldsymbol{\varepsilon}_n + \Delta t\lambda^{\mathrm{vp}}\left(\boldsymbol{\sigma}^{(k)}_{n+1}, T_{n+1}, p^{(k)}_{n+1}\right)\boldsymbol{\Lambda}^{\mathrm{vp}}\left(\boldsymbol{\sigma}^{(k)}_{n+1}\right), \tag{B.4}$$

where k is the iteration counter and where any quantity x is initialized in the current increment using $x^{(0)}_{n+1} = x_n$. Recall that $\boldsymbol{\sigma}$ in a given iteration is calculated from $\boldsymbol{\varepsilon}^{\mathrm{vp}}$ per Hooke's law (2.7). To determine the convergence of the solution (and thus the completion of iteration), we introduce the *viscoplastic strain residual*

$$\mathbf{R}^{(k)}_{n+1} = \boldsymbol{\varepsilon}^{(k)}_{n+1} - \boldsymbol{\varepsilon}^{\mathrm{vp}}_n - \lambda^{\mathrm{vp}}\left(\boldsymbol{\sigma}^{(k)}_{n+1}, T_{n+1}, p^{(k)}_{n+1}\right)\boldsymbol{\Lambda}^{\mathrm{vp}}\left(\boldsymbol{\sigma}^{(k)}_{n+1}\right)\Delta t, \tag{B.5}$$

and iterate until $\left\|\mathbf{R}^{(k)}_{n+1}\right\|$ is less than some tolerance. While the direct iteration method is easily implemented, convergence is only first order and is not in general guaranteed, especially when hardening non-linearities exist (Reddy, 2004). Therefore, we seek a more rigorous method.

---

[11] Here we introduce the notation that, for any quantity x, $\Delta x_{n+1} = x_{n+1} - x_n$.

B.3. Option 3: backward Euler integration (return mapping algorithms)

Another approach to the integration of (B.3) is to rewrite this relation such that the resulting form is implicit with respect to both time steps and iterations. Methods for the implicit integration are well established for plastic and viscoplastic evolution equations (Simo and Hughes, 1998; Ortiz and Popov, 1985; Ortiz and Simo, 1986; Nukala, 2006), and have also been introduced previously in the context of SMA phase transformations (Qidwai and Lagoudas, 2000). Here we consider the class of methods known as return mapping algorithms (RMAs), which can be readily applied to the problem of rate-dependent viscoplasticity provided that the equations can be recast in a form analogous to the rate-independent relations for which these methods were first developed. To that end, we first consider the unknown $\dot{p}$ as analogous to the conventional plastic multiplier, and then use (2.18) to form a relation constraining the value of this unknown (see, for example, the work of Nukala (2006, especially Section 2.3)). This new relation is given as

$$\Phi^{\text{vp}}(\boldsymbol{\sigma}, T, p, \dot{p}) = (\lambda^{\text{vp}}(\boldsymbol{\sigma}, T, p) - \dot{p}) = 0. \tag{B.6}$$

This relation (B.6) acts as a constraint on $\dot{p}$ and as such is analogous to the conventional (rate-independent) consistency condition. Given this, the integration algorithms for classical plasticity can be applied to the viscoplastic problem. Here we consider two algorithms in particular.

B.4. Closest point projection

The process of numerically solving the discretized transformation evolution equation (B.3) directly and implicitly is known as the *closest point projection algorithm* (Simo and Hughes, 1998; Ortiz and Popov, 1985). This method solves (B.3) with all unknowns implicit both in time and in iteration.

Note that, for the case of viscoplasticity only (as is considered currently), the current stress is known in terms of $\boldsymbol{\varepsilon}$, T, and $\boldsymbol{\varepsilon}^{\text{vp}}$, per Hooke's law (2.7). Further, in strain-driven FEA where heat transfer is not considered, $\boldsymbol{\varepsilon}$ and T are known values provided by the global solver. Thus, the two unknown variables to be solved for implicitly are $\{\boldsymbol{\varepsilon}^{\text{vp}}, \dot{p}\}$, and the discretized viscoplastic evolution equation (B.3) becomes

$$\boldsymbol{\varepsilon}_{n+1}^{\text{vp}(k+1)} = \boldsymbol{\varepsilon}_n^{\text{vp}} + \Delta t \dot{p}_{n+1}^{(k+1)} \boldsymbol{\Lambda}^{\text{vp}}\left(\boldsymbol{\sigma}_{n+1}^{(k+1)}\right). \tag{B.7}$$

To find solutions for the unknown scalar $\dot{p}_{n+1}^{(k+1)}$ and the unknown tensor $\boldsymbol{\varepsilon}_{n+1}^{\text{vp}(k+1)}$, we first introduce an iterative update of these two variables per

$$\boldsymbol{\varepsilon}_{n+1}^{\text{vp}(k+1)} = \boldsymbol{\varepsilon}_{n+1}^{\text{vp}(k)} + \Delta\boldsymbol{\varepsilon}_{n+1}^{\text{vp}(k)}; \quad \dot{p}_{n+1}^{(k+1)} = \dot{p}_{n+1}^{(k)} + \Delta\dot{p}_{n+1}^{(k)}, \tag{B.8}$$

where the unknowns are now $\Delta\boldsymbol{\varepsilon}_{n+1}^{\text{vp}(k)}$ and $\Delta\dot{p}_{n+1}^{(k)}$. Linearizing the tensor-valued viscoplastic strain residual $\mathbf{R}$ and the scalar-valued constraint function Φ^{vp} about their roots gives

$$\begin{aligned} \mathbf{R}_{n+1}^{(k+1)} &= \mathbf{R}_{n+1}^{(k)} + \Delta\mathbf{R}_{n+1}^{(k)} \simeq \mathbf{0}, \\ \Phi_{n+1}^{\text{vp}(k+1)} &= \Phi_{n+1}^{\text{vp}(k)} + \Delta\Phi_{n+1}^{\text{vp}(k)} \simeq 0, \end{aligned} \tag{B.9}$$

where $\Delta\mathbf{R}_{n+1}^{(k)}$ and $\Delta\Phi_{n+1}^{\text{vp}(k)}$ are expanded via the chain rule (Simo and Hughes, 1998). The closest point projection algorithm is based on the solution of the system of Eq. (B.9) for the set of unknowns $\left\{\Delta\boldsymbol{\varepsilon}_{n+1}^{\text{vp}(k)}, \Delta\dot{p}_{n+1}^{(k)}\right\}$, which are then used in (B.8).

The resulting algorithm is unconditionally stable and thus will always converge to the correct solution so long as the constraint function is convex (which is the case for the current function Φ^{vp}) (Ortiz and Popov, 1985). It is commonly used in the integration of inelastic constitutive equations (Abaqus, 2007a). However, it has a number of disadvantages relevant to the present work (Simo and Hughes, 1998; Ortiz and Simo, 1986). First, the expansion of $\Delta\mathbf{R}$ via the chain rule requires the evaluation of a number of gradients, some of them being fourth-order tensors, and this "may prove exceedingly laborious" (Ortiz and Simo, 1986). Secondly, while (B.9) represents a 7 × 7 system of equations, the additional consideration of phase transformation phenomena, coupled to the viscoplastic evolution via Hookes law (2.7), doubles the size of the system. Further, the form of these coupled algebraic equations becomes quite complex and the derivation tedious. Finally, the implementation of this algorithm, especially the coupled phase transformation–viscoplastic form, requires a high number of numerical operations per iteration (again, including the evaluation of fourth-order gradient tensors). For these reasons, we explore a slightly simplified form of the return mapping algorithm.

B.5. Convex cutting plane

This method simplifies the closest point projection algorithm by neglecting the iteratively implicit nature of the *direction* of $\boldsymbol{\varepsilon}^{\text{vp}}$ while focusing on its magnitude. According to an original source for this algorithm, it "readily extends to viscoplastic materials" (Ortiz and Simo, 1986). It can be seen that in the case of proportional loading, the direction of strain generation given by $\boldsymbol{\Lambda}_{\text{vp}}$ does not change and the convex cutting plane and closest point projection algorithms become identical. The incremental-iterative form of the discretized evolution equation is then given as

$$\boldsymbol{\varepsilon}_{n+1}^{\mathrm{vp}(k+1)} = \boldsymbol{\varepsilon}_n^{\mathrm{vp}} + \Delta t \dot{p}_{n+1}^{(k+1)} \boldsymbol{\Lambda}^{\mathrm{vp}}\left(\boldsymbol{\sigma}_{n+1}^{(k)}\right). \tag{B.10}$$

Clearly $\boldsymbol{\Lambda}^{\mathrm{vp}}$ is calculated from the solution of the last iteration, but a current solution for $\dot{p}$ must be found. For this we use $(\mathrm{B.8})_2$ and $(\mathrm{B.9})_2$. Considering (B.6) and Hookes law (2.7) where the total strain is provided by the global FEA solver, we then apply the chain rule. This gives

$$\Delta\dot{p}_{n+1}^{(k)} = \frac{-\Phi_{n+1}^{\mathrm{vp}(k)}}{\left(-\partial_{\boldsymbol{\sigma}}\lambda_{n+1}^{\mathrm{vp}(k)} : \mathscr{C}\boldsymbol{\Lambda}^{\mathrm{vp}} + \partial_p \lambda_{n+1}^{\mathrm{vp}(k)}\right)\Delta t - 1}. \tag{B.11}$$

In this way, the backward Euler scheme for integrating the viscoplastic evolution equations is simplified relative to the closest point projection method. The resulting form of the algorithm is convergent provided that the constraint equation is convex in stress, and it converges at a quadratic rate. Further, this convex cutting plane algorithm has been successfully implemented for the integration of the phase transformation evolution equations (Qidwai and Lagoudas, 2000). This is important as a form for the coupled evolution of both processes follows naturally. This coupled evolution of phase transformation and viscoplastic evolution is considered in Section 3.

References

Abaqus, 2007a. Analysis User's Manual. Dassault Systèmes of America Corp., Woodlands Hills, CA.

Abaqus, 2007b. Theory Manual. Dassault Systèmes of America Corp., Woodlands Hills, CA.

Anand, L., Gurtin, M.E., 2003. Thermal effects in the superelasticity of crystalline shape-memory materials. Journal of the Mechanics and Physics of Solids 51, 1015–1058.

Arnold, S., Saleeb, A., Castelli, M., 1996. A fully associative, nonlinear, kinematic, unified viscoplastic model for titanium-based matrices. In: Johnson, W., Larson, J., Cox, B. (Eds.), Life Prediction Methodology for Titanium Matrix Composites, ASTM STP 1253. ASTM.

ASTM, 2000. Standard Test Methods of Compression Testing of Metallic Materials at Room Temperature. ASTM International.

Auricchio, F., Petrini, L., 2004. A three-dimensional model describing stress–temperature induced solid phase transformations: solution algorithm and boundary value problems. International Journal for Numerical Methods in Engineering 61, 807–836.

Auricchio, F., Taylor, R.L., Lubliner, J., 1997. Shape-memory alloys: macromodelling and numerical simulations of the superelastic behavior. Computer Methods in Applied Mechanics and Engineering 146, 281–312.

Auricchio, F., Fugazza, D., DesRoches, R., 2008. Rate-dependent thermo-mechanical modelling of superelastic shape-memory alloys for seismic applications. Journal of Intelligent Material Systems and Structures 19, 47–61.

Bertram, A., 1982. Thermo-mechanical constitutive equations for the description of shape memory effects in alloys. Nuclear Engineering and Design 74, 173–182.

Birman, V., 1997. Review of mechanics of shape memory alloy structures. Applied Mechanics Reviews 50 (11), 629–645.

Boyd, J.G., Lagoudas, D.C., 1996. A thermodynamical constitutive model for shape memory materials. Part I. The monolithic shape memory alloy. International Journal of Plasticity 12 (6), 805–842.

Brinson, L.C., 1993. One-dimensional constitutive behavior of shape memory alloys: thermomechanical derivation with non-constant material functions and redefined martensite internal variable. Journal of Intelligent Material Systems and Structures 4, 229–242.

Chaboche, J., 1997. Thermodynamic formulation of constitutive equations and application to the viscoplasticity and viscoelasticity of metals and polymers. International Journal of Solids and Structures 34 (18), 2239–2254.

Chaboche, J., 2008. A review of some plasticity and viscoplasticity constitutive theories. International Journal of Plasticity 24, 1642–1693.

Coleman, B.D., Gurtin, M.E., 1967. Thermodynamics with internal state variables. The Journal of Chemical Physics 47 (2), 597–613.

Eggeler, G., Khalil-Allafi, J., Neuking, K., Dlouhy, A., 2002. Creep of binary Ni-rich NiTi shape memory alloys and the influence of pre-creep on martensitic transformations. Zeitschrift fur Metallkunde 93, 654–660.

Escobar, J., Clifton, R., 1993. On pressure-shear plate impact for studying the kinetics of stress-induced phase transformations. Material Science & Engineering A 170, 125–142.

Fosdick, R., Ketema, Y., 1998. Shape memory alloys for passive vibration damping. Journal of Intelligent Material Systems and Structures 9, 854–870.

Făciu, C., Mihăilescu-Suliciu, M., 2002. On a rate-type thermomechancial model for shape memory bars. Stress-controlled problems. Zeitschrift fur Angewandte Mathematik und Physik 53, 1014–1025.

Germain, P., 1973. Cours de Mécanique des Miliex Continus: Tome I-Théorie Général. Masson Et Cie, Paris.

Grabe, C., Bruhns, O., 2008. On the viscous and strain rate-dependent behavior of polycrystalline NiTi. International Journal of Solids and Structures 45 (7–8), 1876–1895.

Gurtin, M.E., 1981. An Introduction to Continuum Mechanics. Mathematics in Science and Engineering, vol. 158. Academic Press, San Diego.

Hartl, D., Lagoudas, D., 2009. Constitutive modeling and structural analysis considering simultaneous phase transformation and plastic yield in shape memory alloys. Smart Materials and Structures 18 (1–17).

Hartl, D., Lagoudas, D., Mabe, J., Calkins, F., Mooney, J., 2009. Use of Ni60Ti shape memory alloy for active jet engine chevron application. Part II: experimentally validated numerical analysis. Smart Materials and Structures 19 (1).

Hughes, T.J.R., Winget, J., 1980. Finite rotation effects in numerical integration of rate constitutive equations arising in large-deformation analysis. International Journal for Numerical Methods in Engineering 15 (12), 1862–1867.

Ivshin, I., Pence, T.J., 1994. A thermodynamical model for one-variant shape memory alloy material. Journal of Intelligent Material Systems and Structures 5, 455–473.

Khan, A.S., Huang, S., 1995. Continuum Theory of Plasticity. Wiley, New York.

Kobus, E., Neuking, K., Eggeler, G., 2002. The creep behavior of a NiTi-alloy and the effect of creep deformation on its shape-memory properties. Praktische Metallographie – Practical Metallography 39, 177.

Kumar, P., Lagoudas, D., 2007. Thermomechanical characterization of a TiPdNi high temperature SMA under tension. In: Proceedings of SPIE, Smart Structures and Materials: Behavior and Mechanics of Multifunctional Materials and Composites, San Diego, CA, 19–24 March 6526, pp. 1–10.

Kumar, P., Lagoudas, D., 2009. Creep behavior in TiPdNi high temperature shape memory alloy. In: Proceedings of SPIE, Smart Structures and Materials: Behavior and Mechanics of Multifunctional Materials and Composites III, San Diego, CA, 8–12 March 7289, pp. 1–6.

Lagoudas, D. (Ed.), 2008. Shape Memory Alloys: Modeling and Engineering Applications. Springer, New York.

Lagoudas, D., Entchev, P., 2004. Modeling of transformation-induced plasticity and its effect on the behavior of porous shape memory alloys. Part I: constitutive model for fully dense SMAs. Mechanics of Materials 36 (9), 865–892.

Lagoudas, D.C., Entchev, P.B., Popov, P., Patoor, E., Brinson, L.C., Gao, X., 2006. Shape memory alloys. Part II: modeling of polycrystals. Mechanics of Materials 38 (5–6), 430–462.

Lemaitre, J., Chaboche, J.-L., 1990. Mechanics of Solid Materials. Cambridge University Press, Cambridge.

Lexcellent, C., Rejzner, J., 2000. Modeling of the strain rate effect, creep, and relaxation of a Ni–Ti shape memory alloy under tension (compression)–torsional proportional loading in the pseudoelastic range. Smart Materials and Structures 9, 613–621.

Lexcellent, C., Robinet, P., Bernardini, J., Beke, D., Olier, P., 2005. High temperature creep measurements in equiatomic Ni–Ti shape memory alloy. Materialwissenschaft und Werkstofftechnik 36 (10), 509–512.

Liu, Y., Li, Y., Ramesh, K., 2002. Rate dependence of deformation mechanisms in a shape memory alloy. Philosophical Magazine A 82 (12), 2461–2473.

Machado, L., Savi, M., 2003. Medical applications of shape memory alloys. Brazilian Journal of Medical and Biological Research 36, 683–691.

Machado, L.M., Popov, P., Lagoudas, D.C., submitted for publication. Constitutive model for pollycrystalline shape memory alloys with smooth transformation hardening. International Journal of Engineering Science.

Mantovani, D., 2000. Shape memory alloys: properties and biomedical applications. Journal of the Minerals, Metals and Materials Society 52, 36–44.

Morgan, N., 2004. Medical shape memory alloy applications – the market and its products. Material Science & Engineering A 378, 16–23.

Mukherjee, A., 1968. High-temperature-creep mechanisms of TiNi. Journal of Applied Physics 39 (5), 2201–2204.

Noebe, R., Quackenbush, T.R., Padula, S., 2006. Benchtop demonstration of an adaptive chevron completed using a new high-temperature shape-memory alloy. Tech. Rep. 20060054078, NASA, Glenn Research Center, May 2006.

Nukala, P., 2006. A return mapping algorithm for cyclic viscoplastic constitutive models. Computer Methods in Applied Mechanics and Engineering 195, 148–178.

Odqvist, F., 1966. Mathematical Theory of Creep and Creep Rupture. Clarendon Press, Oxford.

Oppenheimer, S., Yung, A., Dunand, D., 2007. Power-law creep in near-equiatomic nickel–titanium alloys. Acta Materialia 57, 377–380.

Ortiz, M., Popov, E.P., 1985. Accuracy and stability of integration algorithms for elastoplastic constitutive relations. International Journal for Numerical Methods in Engineering 21, 1561–1576.

Ortiz, M., Simo, J., 1986. An analysis of a new class of integration algorithms for elastoplastic constitutive relations. International Journal for Numerical Methods in Engineering 23, 353–366.

Otsuka, K., Wayman, C.M. (Eds.), 1999. Shape Memory Materials. Cambridge University Press, Cambridge.

Padula, S., Bigelow, G., Noebe, R., Gaydosh, D., Garg, A., 2006. Challenges and progress in the development of high-temperature shape memory alloys based on NiTiX compositions for high-force actuator applications. In: Proceedings of the International Conference on Shape Memory and Superelastic Technologies. ASM International, Metals Park, OH.

Paiva, A., Savi, M.A., Bragra, A.M.B., Pacheco, P.M.C.L., 2005. A constitutive model for shape memory alloys considering tensile-compressive asymmetry and plasticity. International Journal of Solids and Structures 42 (11–12), 3439–3457.

Paivia, A., Savi, M., 2006. An overview of constitutive models for shape memory alloys. Mathematical Problems in Engineering 2006, 1–30.

Patoor, E., Lagoudas, D.C., Entchev, P.B., Brinson, L.C., Gao, X., 2006. Shape memory alloys. Part I: general properties and modeling of single crystals. Mechanics of Materials 38 (5–6), 391–429.

Perkins, J., 1975. Shape Memory Effects in Alloys. Plenum Press, New York.

Popov, P., Ravi-Chandar, K., Lagoudas, D., 2003. Dynamic loading of polycrystalline shape memory alloy rods. Mechanics of Materials 35 (7), 689–716.

Qidwai, M.A., Lagoudas, D.C., 2000. Numerical implementation of a shape memory alloy thermomechanical constitutive model using return mapping algorithms. International Journal for Numerical Methods in Engineering 47, 1123–1168.

Raniecki, B., Lexcellent, C., 1998. Thermodynamics of isotropic pseudoelasticity in shape memory alloys. European Journal of Mechanics – A/Solids 17 (2), 185–205.

Reddy, J., 2004. An Introduction to Nonlinear Finite Element Analysis. Oxford University Press, Oxford.

Shaw, J., Kyriakides, S., 1995. Thermomechanical aspects of NiTi. Journal of the Mechanics and Physics of Solids 43 (8), 1243–1281.

Simo, J.C., Hughes, T.J.R., 1998. Computational inelasticity. Interdisciplinary Applied Mathematics, vol. 7. Springer, New York.

Srinivasan, A.V., McFarland, D., 2000. Smart Structures: Analysis and Design. Cambridge University Press, Cambridge.

Stebner, A., Padula, S., Noebe, R., Lerch, B., Quinn, D., 2009. Development, characterization, and design considerations of Ni19.5Ti50.5Pd25Pt5 high-temperature shape memory alloy helical actuators. Journal of Intelligent Material Systems and Structures 20, 2107–2120.

Tanaka, K., Kobayashi, S., Sato, Y., 1986. Thermomechanics of transformation pseudoelasticity and shape memory effect in alloys. International Journal of Plasticity 2, 59–72.

Toi, Y., Lee, J.-B., Taya, M., 2004. Finite element analysis of superelastic, large deformation behavior of shape memory alloy helical springs. Computers and Structures 82, 1685–1693.

Wang, X., Xu, B.X., Yue, Z., 2008. Micromechanical modelling of the effect of plastic deformation on the mechanical behavior in pseudoelastic shape memory alloys. International Journal of Plasticity 24, 1307–1332.

Yan, W., Wang, C., Zhang, X., Mai, Y., 2003. Theoretical modeling of the effect of plasticity on reverse transformation in superelastic shape memory alloys. Material Science & Engineering A A354, 146–157.

Zhang, Y., Cheng, Y., Grummon, D., 2007. Finite element modeling of indentation-induced superelastic effect using a three-dimensional constitutive model for shape memory materials with plasticity. Journal of Applied Physics 101 (053507), 1–6.